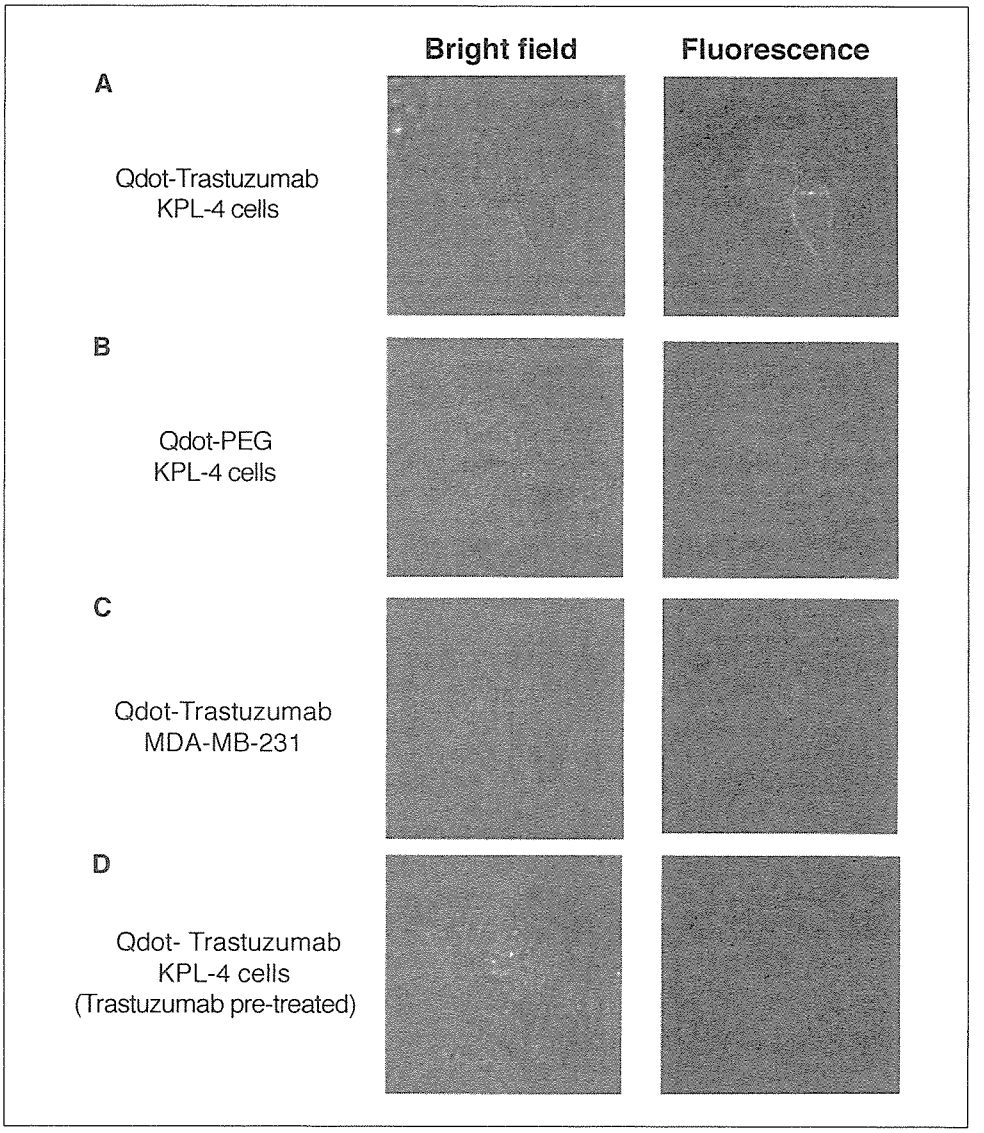

Figure 1. Immunocytochemical studies of QT-complex binding activity in cultured breast cancer cells. *A*, KPL-4 cells, which are HER2 positive, as revealed by the presence of the QT complex on the cell surface. *B*, negative staining was detected in KPL-4 cells exposed to QD-PEG in the absence of anti-HER2 antibody. *C*, negative staining was detected in MDA-MB-231 cells, which are HER2 negative. *D*, competition study of QT complex and trastuzumab. After addition of 100 nmol/L trastuzumab to KPL-4 cells, QT-complex fluorescence was absent. QT-complex fluorescence was detected on the cell surface of KPL-4 but not MDA-MB-231, confirming HER2 as a cell surface–specific marker for some breast cancer cell lines.

it has been found to have little or no effect on their binding ability. QT complex [Qdot (Q)-trastuzumab (T) complex] was fractionated by agarose gel electrophoresis into three major bands. Approximately 60% of the QT complex was conjugated with three antibody fragments, ~30% with two fragments, and ~10% with a single fragment (data not shown).

The final concentration of QT complexes was determined by measuring the conjugate absorbance at 550 nm and using an extinction coefficient of 1,700,000 M^{-1} cm^{-1} at 550 nm.

Cell line and mouse model. The human breast cancer cell line KPL-4, which overexpresses HER2 and is sensitive to trastuzumab (15, 16), was kindly provided by Dr. J. Kurebayashi (Kawasaki Medical school, Kurashiki, Japan). KPL-4 cells were cultured in DMEM supplemented with 5% fetal bovine serum (FBS). MDA-MB-231 cells were maintained in RPMI with 10% FBS. Conventional immunohistochemical procedures were used to determine the binding of QT-complex conjugate to KPL-4 cells, using both QD-PEG (no antibody) and MDA-MB-231 as negative controls. In these studies, QT-complex or QD-PEG bioconjugates (100 nmol/L) were incubated with the cells for 30 min at 37°C, washed, and photographed. For competition study of QT complex and trastuzumab, KPL-4 was pretreated with trastuzumab (100 nmol/L) for 30 min before exposure to 100 nmol/L QT complex.

A suspension of KPL-4 cells (0.8×10^7 per mouse) was transplanted s.c. to the dorsal skin of female BALB/c *nu/nu* mice at 6 to 10 weeks of age (Charles River Japan, Yokohama, Japan). Several weeks after tumor inoculation, mice bearing a tumor volume of 100 to 200 mm^3 were selected. All of the mice were maintained in our pathogen-free institutional facilities. All operations on animals were in accordance with the institutional animal use and care regulations.

QT complexes were injected into the tail vein of mice at a concentration of 2 μmol/L and a volume of 100 μL. The mice were placed under anesthesia by the i.p. injection of a ketamine and xylazine mixture at dosages of 95 and 5 mg/kg, respectively. The temperature of mice was maintained at 37°C with a thermoplate and objective lens heater.

The dorsal skinfold chamber, previously described (13) and modified for this study, was used to fix the exposed mouse tumor on the stage of the microscope. Two sterilized polyvinyl chloride plates (0.5-mm thickness) containing a window were mounted to fix the extended double layer of dorsal skin including the tumor site. Skin between chambers was sutured together with 6-0 nylon around the window so the tumor could be located in the center of the window and fixed without influence from the beating of the heart and/or breathing. The tumor was exposed by oval incision of ~10-mm diameter, and the s.c. connective tissue was removed. The tumor was then placed surface down in neutral saline, mounted on coverslip, and viewed under an inverted microscope. The mouse was fixed to a metal plate on the stage designed to stabilize the chamber. Tumors can be visualized directly by means of this setup.

After imaging, the mice were sacrificed by CO_2 overdose. The tumors were removed and divided for histologic Qdot uptake study and immunohistochemical analysis. For the histologic Qdot uptake study, tumors were frozen and cryosectioned (6-μm thickness), fixed with acetone at 0°C, and examined with an imaging system. For immunohistologic examination, tumors were fixed in 10% neutral-buffered formalin overnight and then transferred to ethanol before processing and paraffin embedding. Immunohistochemical analysis was done on paraffin sections of 6-mm thickness using the HercepTest (DakoCytomation, Carpinteria, CA).

***In vivo* imaging and tracking.** *Optics and image analysis:* The optics system for three-dimensional observation consisted primarily of an epifluorescent microscope (IX71, Olympus, Tokyo, Japan) with modifications (17, 18), a Nipkow lens type confocal unit (CSU10, Yokokawa, Japan), and an electron multiplier type CCD camera (iXon 887, Andor, Tokyo, Japan). The confocal unit adopts multibeam scanning using about a thousand beams that are simultaneously emitted through a pin-hole disk to facilitate high-speed scanning. The EMCCD has an advantage that offers unsurpassed sensitivity performance and has been shown to yield markedly improved S/N (signal/noise) ratio (14). The object lens (60×, numerical aperture 1.45) was moved by a piezo actuator with a feedback loop (Nanocontrol) for stabilizing the position of the focus. A computer controlled the piezo actuator in synchronization with the image acquisitions that the object lens remained within the exposure time of the CCD camera. An area of ~ 30 × 30 μm^2 was illuminated by a green laser (532 nm, CrystaLaser, Reno, NV). This system captures images of single Qdot at a video rate of 33 ms/frame. Three-dimensional confocal intravital images of single QT complex were taken by moving an objective lens (Fig. 2*A*). Three-dimensional images of the tumor were taken by reconstructing 10 to 20 confocal images from the surface of the mice to a depth of 150 μm inside the tumor through the DSFC.

The *xy* position of the fluorescent spot was calculated by fitting to a two-dimensional Gaussian curve. The single molecule could be identified by the fluorescence intensity. In addition, quantitative and qualitative information such as velocity, directionality, and transport mode was obtained using time-resolved trajectories of particles. The resolution of the position was determined from the position of immobile QT complexes in a chemically fixed tumor cell. The resolution of the *x* and *y* directions of images taken at an exposure time of 33 ms was 30 nm, taking into consideration the SD.

Results and Discussions

***In vitro* study.** Qdots were conjugated to trastuzumab using the Qdot-antibody conjugation kit (QT complex). Immunocytochemical data confirmed strong and specific binding of the QT complex to a HER2-overexpressing human breast cancer cell line (Fig. 1*A*). QD-PEG without antibody showed almost no binding to KPL-4 cells (Fig. 1*B*). MDA-MB-231, a HER2 negative human breast cancer cell line, showed the absence of Qdot binding (Fig. 1*C*). KPL-4 cells pretreated by excess trastuzumab also showed the absence of Qdot binding (Fig. 1*D*). These results indicate that QT complexes selectively bind to the HER2 protein. Furthermore, QT complex was compared with trastuzumab labeled with rhodamine, which is recognized as similar to native trastuzumab. Both QT complex and rhodamine-trastuzumab bound to the KPL-4 cell at concentrations of 1 nmol/L but hardly at 0.1 nmol/L, indicating the binding properties of QT complex are similar to those of native antibody (data not shown).

Three-dimensional imaging of single Qdot-trastuzumab in mice. It is reported that the accumulation of trastuzumab at the HER2-overexpressing tumor site in mice model is the basis for radioimmunoscintigraphic scanning and targeted therapy for human HER2-overexpressing breast cancer (19–21). Here tumor-bearing mouse models were prepared with KPL-4 s.c. implantation. The QT complex accumulated in the tumor specifically because only the tumor area generated fluorescence of Qdots (Supplementary Fig. S1*A* and *B*). Single Qdots in the mice tumor were observed using a high-resolution intravital imaging system through the dorsal skinfold chamber (Fig. 2*A*; ref. 13). Fluorescence microangiography was done after injection of the QT complexes into the tail vein. After injection, blood sample from mice was examined by fluorescence observation on whether QT complex had made the aggregation in the mice. QT complex existed as a single particle without further aggregation (data not shown). The membranes of the KPL-4 tumor cells were clearly stained with single QT complexes at 6 h after the injection. At 24 h after the injection, the QT complexes had been internalized into the tumor cells (Fig. 2*B* and *C*). After imaging of the tumors in the living mice, histologic examination of the chemically fixed tumors was done to confirm that QT complexes in the living mice exhibit activity in KPL-4 cells. QT complexes observed under a three-dimensional microscope were located at the cell membrane and near the nuclear membrane (Supplementary Fig. S2*A* and *B*). An adjacent slice of the observed area was further stained

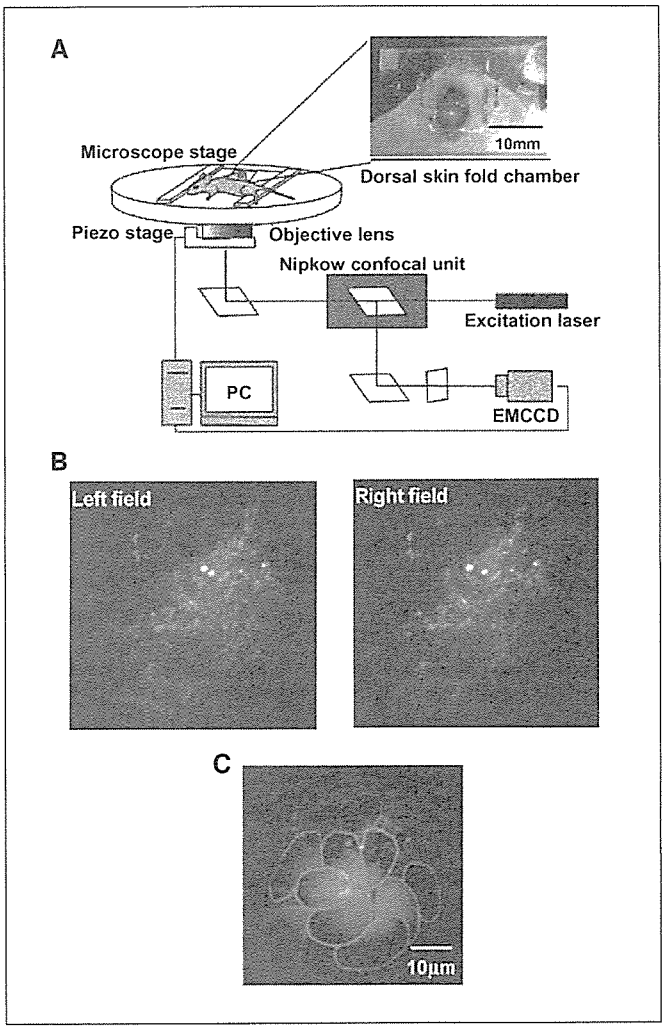

Figure 2. Experimental diagram and three-dimensional intravital cancer imaging. Mice prepared for dorsal skinfold chamber were fixed on the microscopic stage. QT complexes were injected into the tail vein of nude BALB/c mice bearing KPL-4 breast cancer xenograft tumor. *A*, three-dimensional microscopic system consisting of a confocal unit, an EMCCD, and a computer to control the piezo stage. *B*, three-dimensional image of the tumor was obtained by the QT complexes binding to tumor cell membrane (stereoscopic image: left and right field). *C*, traced outlines of the cells shown in (*B*).

immunohistochemically with the anti-HER2 antibody A0485. The cell membrane stained locally in the adjacent slice (Supplementary Fig. S2*C*), confirming that QT complexes were present on the membrane of tumor cells.

Extravasation of single QT complexes in tumors of mice with two-dimensional imaging. After the injection, three-dimensional images of the tumor were taken to allow observation on the tumor vessel of single QT complexes. The position of the objective was fixed and 300 to 3,000 sequential confocal two-dimensional images (total, 10–100 s) were taken at this fixed position. Within 30 s after the injection, the current of the QT complex in a vessel was observed. When the vessel and cells were clearly observable, the the current of single QT complex in the tumor vessel was then analyzed. The fluorescent image of the circulating QT complex was not a circle but an ellipse and sometimes a line at the video rate because QT complex at times moved >1 μm in single frame. The speed of the movement of the single particles was calculated from the positional changes of the centroid of the QT complex images (Fig. 3*A*). The average speed of each complex ranged from 100 to 600 μm/s, in agreement with a previous report by another method (22). As shown in Fig. 3*A*, each particle exhibits slow and fast movement in the bloodstream. Such fast and slow movement characteristics could be induced by the pulse and nonuniform current within a vessel such as the Hagen-Poiseuille current. The slow speed of the complexes inside a tumor vessel would be important to locate pores between the vessel cells and then the complexes diffuse out from these pores.

Focusing on the vessel walls, a movement was observed of the complex extravasated from the intravascular space (Fig. 3*B*). The edge of the vascular inner surface was not clear on a single frame image. Therefore, all the images obtained were averaged to precisely determine the position of the edge (Fig. 3*B*, *i–iii*). The complexes were positioned first on the vascular surface and then extravasated. This is the first example of video rate observation of extravasation of very small particles, such as Qdots, in a mouse model. The moving speed of the complexes was very low, 1 to 4 μm/s, at the pore of the vascular cells, compared with the speed in the current. The QT complexes either interacted with the vascular cells or became trapped in the extracellular matrix.

Diffusion of single QT complexes in extracellular and intercellular regions. Two hours after the injection, many complexes had migrated into the tumor interstitial area close to the tumor vessels. Most of the movement of the complexes was random in orientation and speed, indicating that complexes diffuse by the Brownian motion exerted by thermal energy. The average diffusion coefficient of the complexes was 0.0014 $\mu m^2/s$, much smaller than that at free diffusion in solution (~ 10 $\mu m^2/s$). Many complexes also moved randomly within a restricted small area of ~ 1-μm diameter and then hopped by ~ 1 μm (Fig. 4*A*). These results indicate that movement is restricted by a cage formed by the extracellular matrix and, at times, complexes escape from this cage.

Binding of QT complexes to cell membrane and vesicle transport. Six hours after the injection, QT complexes had bound to the KPL-4 cell membrane on which the HER2 protein is located. We successfully captured specific images of the QT complexes bound to the cell membrane (Fig. 4*B*). Movements of single QT complex are identified in single frames. To identify the positions of the tumor vessels and cells in living mice without further fluorescence staining, images were averaged (Supplementary Fig. S3*A*). As viewed from the outside of the delineated cells, the QT complexes moved toward the cell membrane at a speed of 200 to 400 nm/s (Fig. 4*C*), remained on the membrane for a few seconds, and then moved randomly along the membrane. QT complexes moved between the cells, bound to HER2, and then moved in association with HER2 on the membrane.

Many QT complexes bound to the cell membrane exhibited Brownian motion within a restricted region of ~ 500-nm diameter. The region is significantly larger than the area of ~ 30 nm, which was drawn by position noise of the complexes fixed on a coverslip, indicating the movement is due to the anchor of the HER2 to a flexible component of the cytoskeleton such as an actin filament (23). The QT complexes restricted to the small area initiated linear movement in one direction along the cell membrane with a speed of 400 to 600 nm/s and traveled for several micrometers (Fig. 5*A* and *B*; Supplementary Fig. S3*B*).

We also succeeded in pursuing the transport of QT complexes from the peripheral region of the cell to the perinuclear region

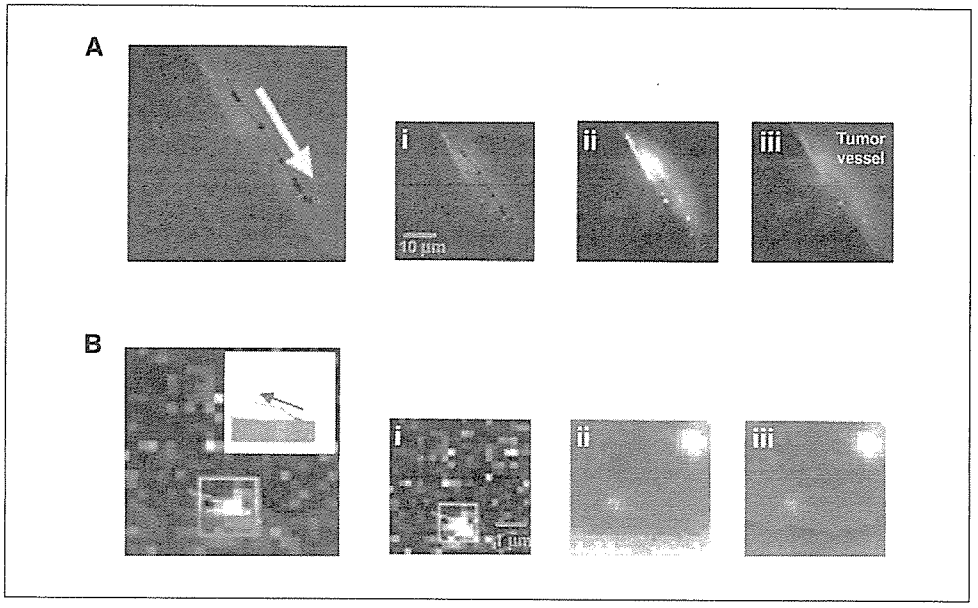

Figure 3. The movement of QT complexes from tumor vessels to the interstitial space. *A*, flow of QT complexes in the tumor vessel. The speed was calculated by the moving distance per 33 ms. The maximum speed was ~600 μm/s. *B*, extravasation of QT complexes from the vascular space of the tumor. *Dotted line*, trajectory of the extravasation. *i*, an initial single frame tracing the trajectory of a single QT complex shown as a dotted line at video rate. *ii*, sequential frames were averaged to define the edge of vessel. *iii*, tracing of the outlines of tumor vessels. Overlapping initial single image and (*iii*), the tracing image gives the final images. *B*, *inset*, magnified image of the trajectory of extravasating QT complex.

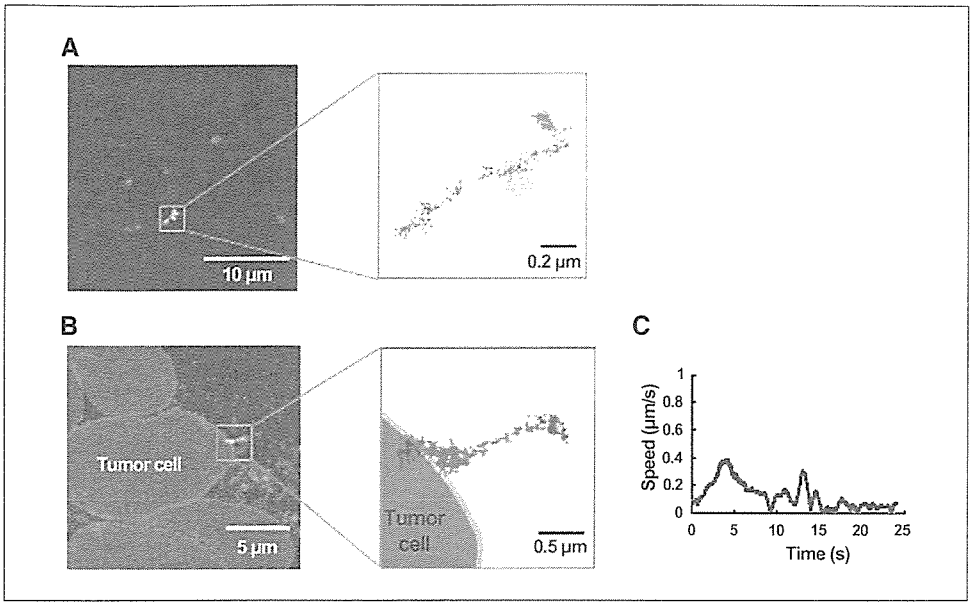

Figure 4. Tracking the movement of QT complexes from the interstitial space to the cell membrane. *A*, trajectory of the QT complexes in the interstitial space near the tumor vessels and magnified trajectory. The color of the trajectory codes the time axis from black to pink, yellow, and light blue. *B*, trajectory of the binding to the cell membrane and magnified trajectory. *C*, time trajectory of the velocity of (*B*). The color of the trajectory of both (*B*) and (*C*) codes the time axis from blue to red and green. All time trajectories of the velocity are calculated by the least squares method (2 s).

(Fig. 5*C*; Supplementary Fig. S3*C*). The QT complex in a given cell moved almost straight toward the cell membrane with a velocity of 100 to 300 nm/s, changed direction to parallel to the cell membrane, and moved toward the cell nucleus at a velocity of ~600 nm/s (Fig. 5*D*). Finally, the directional movement of the QT complexes ceased and Brownian motion commenced within a small area, ~1 μm in a diameter, near the nucleus (Fig. 5*C* and *D*, *black line*). The first two movements of straight toward and along the cell membrane would most likely be produced by the transport of an acto-myosin system binding to vesicle containing QT complexes (24, 25). Because the actin filaments in cultured cells are highly concentrated in the peripheral region of cells, movement toward the nucleus would most likely be on a microtubule transported by dynein (26) as there are almost no actin filaments near nucleus, but rather, a high concentration of microtubules.

Summary of the delivery processes. We have succeeded in capturing the specific delivery of single QT complexes in tumor vessels to the perinuclear region of tumor cells in live mice after QT complexes had been injected into the tail vein of mice. Six stages were detected (Fig. 6): (*a*) vessel circulation, (*b*) extravasation, (*c*) movement into the extracellular region, (*d*) binding to HER2 on the cell membrane, (*e*) movement from the cell membrane to the perinuclear region after endocytosis, and (*f*) in the perinuclear region. The translational speed of QT complexes in each process was highly variable, even in the vessel circulation. The movement of the complexes in each process was also found to be "stop-and-go" (i.e., the complex remaining within a highly restricted area and then moving suddenly). This indicates that the movement was promoted by a motive power and constrained by both the three-dimensional structure and protein-protein interactions. The motive

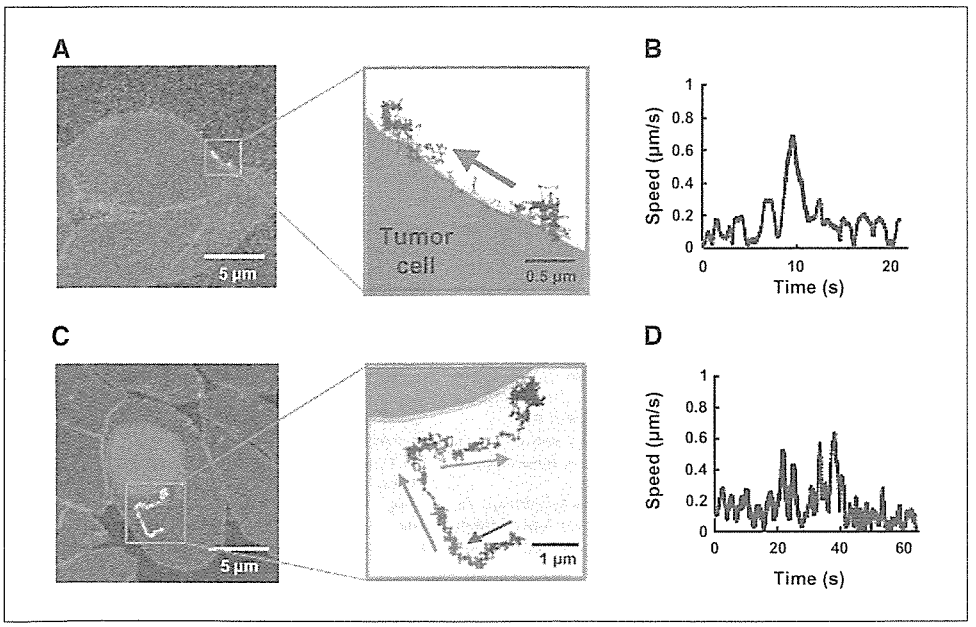

Figure 5. Tracking of the movement of QT complexes from the cell membrane to the perinuclear region. *A*, trajectory of the QT complexes binding to the cell membrane and magnified image. *B*, time trajectory of the velocity of (*A*). The color of the trajectory of both (*A*) and (*B*) codes the time axis from blue to red and green. *C*, trajectory of the intracellular transport of QT complex and magnified image. *D*, time trajectory of the velocity of (*C*). The color of the trajectory of both (*C*) and (*D*) codes the time axis from blue to red, green, and black. All time trajectories of the velocity are calculated by the least squares method (2 s).

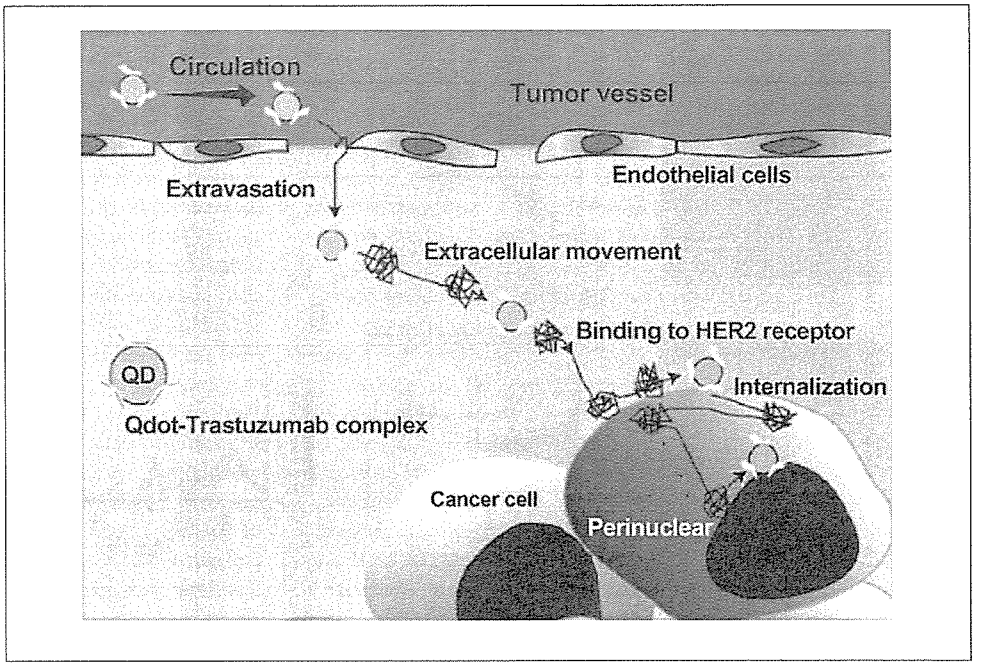

Figure 6. Schematic illustration of the QT complex, the QT complex entered into the circulation, extravasated into the interstitial space from the vascular space, bound to the tumor cells through the interstitial region, and having reached the perinuclear region after traveling on the intracellular rail protein. All processes exhibit a characteristic "stop-and-go" movement.

power of the movements was produced by blood circulation (essential in processes *a* and *b*), diffusion force driven by thermal energy (*b*, *c*, and *d*), and active transport by motor proteins (*e*). The cessation of movement is most likely induced by a structural barricade such as a matrix cage (*b*, *c*, and *f*) and/or specific interaction between proteins (e.g., an antibody) and HER2 (*d*), motor proteins, and rail filaments such as actin filaments and microtubules (*e*).

The molecular mechanism underlying the movement and its cessation during delivery of nanoparticles in animal models is the fundamental basis of drug delivery. There have been many different approaches to tumor-targeting "nanocarriers" including anticancer drugs for passive targeting, such as Myocet (27) and Doxil (28), and for active targeting, such as MCC-465 (29) and anti-HER2 immunoliposome (19). There is still very little understanding of the biological behavior of nanocarriers, including such crucial features as their transport in the blood circulation, cellular recognition, translocation into the cytoplasm, and final fate in the target cell. These results suggest that the transport of nanocarriers would be quantitatively analyzable in the tumors of living animals by the present method. This approach should thus afford a potential new insight into particle behavior in complex biological environments. Such new insight in turn will allow rational improvements in particle design to increase the therapeutic index of the tumor-targeting nanocarriers.

Acknowledgments

Received 4/4/2006; revised 8/24/2006; accepted 12/5/2006.

Grant support: Grants-in-aid for Research Project; Promotion of Advanced Medical Technology (H14-Nano-010, H18-Nano-General-001); Ministry of Health, Labor, and Welfare of Japan (N. Ohuchi); Scientific Research in Priority Areas from the Japan MEXT and CREST from the JST (H. Higuchi); and Special Coordination Funds for Promoting Science and Technology of Japan (H. Higuchi and T.M. Wanatabe).

The costs of publication of this article were defrayed in part by the payment of page charges. This article must therefore be hereby marked *advertisement* in accordance with 18 U.S.C. Section 1734 solely to indicate this fact.

We thank Dr. H.A. Nguyen for helpful discussion and Dr. J.M. West for critical reading of the manuscript.

References

1. Mamot C, Drummond DC, Noble CO, et al. Epidermal growth factor receptor-targeted immunoliposomes significantly enhance the efficacy of multiple anticancer drugs *in vivo*. Cancer Res 2005;65:11631–8.
2. Torchilin VP, Lukyanov AN, Gao Z, Papahadjopoulos-Sternberg B. Immunomicelles: targeted pharmaceutical carriers for poorly soluble drugs. Proc Natl Acad Sci U S A 2003;100:6039–44.
3. Krauss WC, Park JW, Kirpotin DB, Hong K, Benz CC. Emerging antibody-based HER2 (ErbB-2/neu) therapeutics. Breast Dis 2000;11:113–24.
4. Ishijima A, Kojima H, Funatsu T, et al. Simultaneous observation of individual ATPase and mechanical events by a single myosin molecule during interaction with actin. Cell 1998;92:161–71.
5. Lyons SK. Advances in imaging mouse tumour models *in vivo*. J Pathol 2005;205:194–205.
6. Wu X, Liu H, Liu J, et al. Immunofluorescent labeling of cancer marker Her2 and other cellular targets with semiconductor quantum dots. Nat Biotechnol 2003;21:41–6.
7. Bruchez M, Jr., Moronne M, Gin P, Weiss S, Alivisatos AP. Semiconductor nanocrystals as fluorescent biological labels. Science 1998;281:2013–6.
8. Gao X, Cui Y, Levenson RM, Chung LW, Nie S. *In vivo* cancer targeting and imaging with semiconductor quantum dots. Nat Biotechnol 2004;22:969–76.
9. Endow SA, Higuchi H. A mutant of the motor protein kinesin that moves in both directions on microtubules. Nature 2000;406:913–6.
10. Yildiz A, Forkey JN, McKinney SA, Ha T, Goldman YE, Selvin PR. Myosin V walks hand-over-hand: single fluorophore imaging with 1.5-nm localization. Science 2003;300:2061–5.
11. Dahan M, Levi S, Luccardini C, Rostaing P, Riveau B, Triller A. Diffusion dynamics of glycine receptors revealed by single-quantum dot tracking. Science 2003;302:442–5.
12. Lidke DS, Nagy P, Heintzmann R, et al. Quantum dot ligands provide new insights into erbB/HER receptor-mediated signal transduction. Nat Biotechnol 2004;22:198–203.
13. Leunig M, Yuan F, Menger MD, et al. Angiogenesis, microvascular architecture, microhemodynamics, and interstitial fluid pressure during early growth of human adenocarcinoma LS174T in SCID mice. Cancer Res 1992;52:6553–60.
14. Chong FK, Coates CG, Denvir DJ, McHale NG, Thornvury KD, Hollywood MK. Optimization of spinning disk confocal microscopy: synchronization with the ultra-sensitive EMCCD. Proc SPIE 2004;5324:65–76.
15. Kurebayashi J, Otsuki T, Tang CK, et al. Isolation and characterization of a new human breast cancer cell line, KPL-4, expressing the Erb B family receptors and interleukin-6. Br J Cancer 1999;79:707–17.

16. Fujimoto-Ouchi K, Sekiguchi F, Tanaka Y. Antitumor activity of combinations of anti-HER-2 antibody trastuzumab and oral fluoropyrimidines capecitabine/5′-dFUrd in human breast cancer models. Cancer Chemother Pharmacol 2002;49:211–6.
17. Nguyen VT, Kamio Y, Higuchi H. Single-molecule imaging of cooperative assembly of γ-hemolysin on erythrocyte membranes. EMBO J 2003;22:4968–79.
18. Nguyen H, Higuchi H. Motility of myosin V regulated by the dissociation of single calmodulin. Nat Struct Mol Biol 2005;12:127–32.
19. Park JW, Kirpotin DB, Hong K, et al. Tumor targeting using anti-her2 immunoliposomes. J Control Release 2001;74:95–113.
20. Ballangrud AM, Yang WH, Palm S, et al. α-Particle emitting atomic generator (Actinium-225)-labeled trastuzumab (Herceptin) targeting of breast cancer spheroids: efficacy versus HER2/neu expression. Clin Cancer Res 2004;10:4489–97.
21. Wiercioch R, Balcerczak E, Byszewska E, Mirowski M. Uptake of radiolabelled Herceptin by experimental mammary adenocarcinoma. Nucl Med Rev Cent East Eur 2003;6:99–103.
22. Braun RD, Abbas A, Bukhari SO, Wilson W III. Hemodynamic parameters in blood vessels in choroidal melanoma xenografts and rat choroid. Invest Ophthalmol Vis Sci 2002;43:3045–52.
23. Carraway CA, Carvajal ME, Carraway KL. Association of the Ras to mitogen-activated protein kinase signal transduction pathway with microfilaments. Evidence for a p185(neu)-containing cell surface signal transduction particle linking the mitogenic pathway to a membrane-microfilament association site. J Biol Chem 1999;274:25659–67.
24. Buss F, Arden SD, Lindsay M, Luzio JP, Kendrick-Jones J. Myosin VI isoform localized to clathrin-coated vesicles with a role in clathrin-mediated endocytosis. EMBO J 2001;20:3676–84.
25. Aschenbrenner L, Naccache SN, Hasson T. Uncoated endocytic vesicles require the unconventional myosin, Myo6, for rapid transport through actin barriers. Mol Biol Cell 2004;15:2253–63.
26. Kamal A, Goldstein LS. Connecting vesicle transport to the cytoskeleton. Curr Opin Cell Biol 2000;12:503–8.
27. Mross K, Niemann B, Massing U, et al. Pharmacokinetics of liposomal doxorubicin (TLC-D99; Myocet) in patients with solid tumors: an open-label, single-dose study. Cancer Chemother Pharmacol 2004;54:514–24.
28. O'Brien ME, Wigler N, Inbar M, et al. Reduced cardiotoxicity and comparable efficacy in a phase III trial of pegylated liposomal doxorubicin HCl (CAELYX/Doxil) versus conventional doxorubicin for first-line treatment of metastatic breast cancer. Ann Oncol 2004;15:440–9.
29. Hamaguchi T, Matsumura Y, Nakanishi Y, et al. Antitumor effect of MCC-465, pegylated liposomal doxorubicin tagged with newly developed monoclonal antibody GAH, in colorectal cancer xenografts. Cancer Sci 2004;95:608–13.

Fluorescence tomography in turbid media based on acousto-optic modulation imaging

Masaki Kobayashi,[a] Takashi Mizumoto, Yukihiro Shibuya, and Masaru Enomoto
Department of Electronics, Tohoku Institute of Technology, Sendai 982-8577, Japan

Motohiro Takeda
Department of Bioengineering and Robotics, Graduate School of Engineering, Tohoku University, Sendai 980-8579, Japan

(Received 4 June 2006; accepted 7 September 2006; published online 30 October 2006)

The authors present a tomographic imaging technique of fluorescence in light-scattering media. Ultrasonic modulation of fluorescence based on the interaction between ultrasound and light is applied for imaging of a fluorescent material by scanning a focused sound field in which the light is modulated selectively. The on-axis sound-field characteristics that affect the light by modulating its amplitude (through variation of the refractive index and the scattering coefficient) were determined. That imaging technique is demonstrated using tissue phantoms that contain localized fluorescent regions in a dense scattering medium, suggesting the applicability of this technique for visualization of fluorescent probes in biological tissues. © *2006 American Institute of Physics*. [DOI: 10.1063/1.2364600]

Fluorescence imaging techniques that are employed in studies of life sciences have become increasingly important for assays of biological functions. Widely various fluorescent probes that are designed to be combined with target molecules, as well as a technique including genetic modification that produces fluorescent proteins, have been commonly used for visualization of dynamics of biofunctions that emerge in sites of vital phenomena in real time. Particularly, fluorescence techniques are the most powerful methods for visualization of cellular functions at the microscopic level. However, at the macroscopic level, light-scattering properties of biological tissues restrict the range of optical methods' applicability for investigations inside living bodies. A great deal of effort has been devoted to development of optical imaging in living bodies. Those efforts have improved characterization of the spatial distribution of optical properties. Time and frequency domain techniques[1] using near-infrared light characterizing diffuse light and coherent-gating[2,3] technique to extract the straightforward scattered light can facilitate tomographic imaging of biological tissues. Recently, *tagging* technique, which extracts optical information using some other physical energy, such as ultrasound, has garnered attention. Ultrasound tagging technique was demonstrated for extraction of optical absorption properties with assistance of less-scattered ultrasonic waves.[4–6] This technique is based on intensity modulation through fluctuation of speckles formed by multiply scattered coherent light in a varying sound-pressure field. By this principle, optical coherent properties are crucial for light modulation. However, displacement of scattering particles and variation of the refractive index that is induced by density distribution in a sound field might engender the intensity modulation of scattered light, even in incoherent light. In the tagging technique, which measures optical absorption, the incoherent modulation component is generally undetectable because the modulated component is too small in comparison to the unmodulated component of multiply scattered light.[7] However, for fluorescence measurement, the modulated component of fluorescence that is excited with modulated incoherent light is potentially detectable because of the spectral distinction between fluorescence and excitation wavelength under the appropriate optical arrangement of a detector for highly efficient light collection. In this letter, we demonstrate tomographic imaging of fluorescence in dense scattering media using tissue phantoms that involve small, localized fluorescent regions.

Figure 1 shows that the experimental setup comprises a continuous wave diode pumped solid state laser system (Verdi V-6; Coherent, Inc.) as a light source, an ultrasound transducer, and a photomultiplier tube (PMT) as a detector. The laser beam is reduced and collimated to 1 mm diameter and enters the water tank through a glass window. A focus-type ultrasonic transducer (38 mm focal length, 3 mm focal diameter, V314-SU; Olympus-NDT) that is driven by a 1 MHz continuous sinusoidal wave is incorporated into the

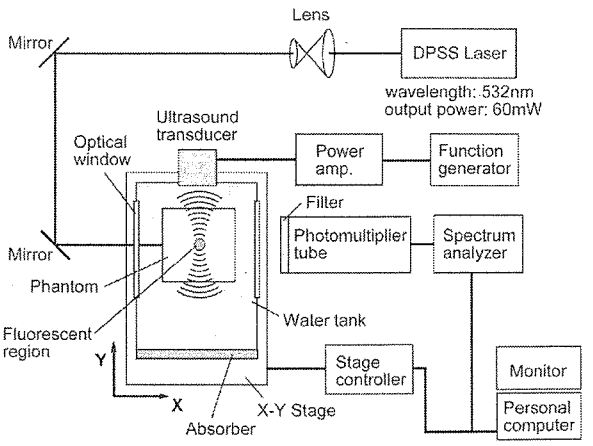

FIG. 1. (Color online) Schematic of the experimental setup. A water tank equipped with an ultrasound transducer is set on the *X-Y* autostage; a tissue phantom is fixed in place without touching the water tank.

[a]Electronic mail: masaki@tohtech.ac.jp

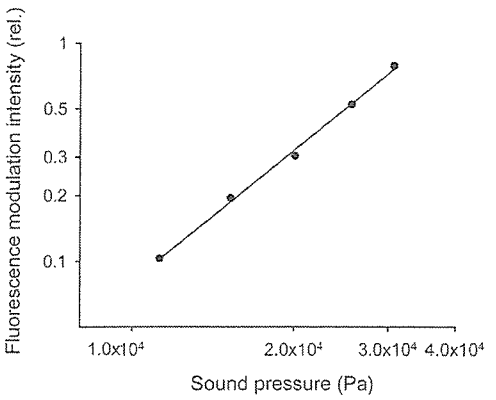

FIG. 2. Characteristics of fluorescence modulation intensity vs sound pressure in the ultrasound focus. Measurements were carried out while varying the excitation voltage applied to an ultrasound transducer focused on the fluorescent pigment in a tissue phantom.

side wall of the water tank, where the ultrasound beam traverses the incident axis of the laser beam. Sound pressure in the sound-field focus region was 4.1×10^4 Pa in water. The signal from the PMT is fed into a spectrum analyzer and the intensities of the resonant frequencies are detected using a narrow bandwidth (100 Hz). To obtain a two-dimensional tomographic image of fluorescence intensity through scanning of the ultrasound focus, a water tank equipped with a transducer is mounted on a two-axis translational stage and scanned in 500 μm steps along the X axis (parallel to the incident laser beam) and the Y axis (parallel to the ultrasound beam). It is controlled using a personal computer that is synchronized with a spectrum analyzer. A tissue phantom is suspended independently from the holder, which is located above the water tank; the phantom is immersed in the water without touching the water tank. The optical arrangement of the phantom and incident light remains unchanged during scanning of the ultrasound beam. The imaging experiments are conducted using a wavelength of 532 nm and an incident beam signal intensity of 60 mW.

The light modulation mechanism is inferred to be induced through density variation of the medium in the ultrasound field, which engenders changes of the refractive index and optical scattering coefficient. When fluorescent pigment is present in the sound field, the density variation of the medium engenders modulation of the photon density through deflection of light between two successive scattering events in the gradient of the refractive index, thereby causing fluorescence intensity modulation. Variation of the scattering coefficient also causes modulation of the fluorescence intensity.

Throughout the experiments, we used gel tissue phantoms of isotropic light-scattering media made of 5% agar (Inagel; Ina Food Industry Co. Ltd., Nagano, Japan) that were prepared through dilution of Intralipid (Intralipid 10%; Fresenius Kabi AG, Germany), which is a clinically useful fat emulsion that is often used for tissue phantom studies to elucidate light propagation in scattering media. The final volume concentration of Intralipid in the phantom was 40 ml/l in 5% agarose gel with the water-glycerin (20%) solution. The agarose gel was molded to $40\times40\times75$ mm^3. A fluorescent region in the phantom was formed by embedding a fluorescent material that contains fluorescent microspheres (530 nm absorption peak, 590 nm emission wavelength, fluoresbrite carboxylate microspheres, NYO; Polyscience, USA) molded with columnar agarose gel (5 mm long, 3 mm diameter). The reduced scattering coefficient of the phantom was estimated as 0.61 mm^{-1} at the excitation wavelength.

Figure 2 shows characteristics of fluorescence modulation intensity in the scattering medium versus sound pressure in the ultrasound focus. Data were measured while varying the excitation voltage of the transducer at the position where the ultrasound focus corresponds to the fluorescent region site. Fluorescence modulation (signal) intensity is proportional to the square of the sound pressure, indicating a linear relationship between the sound power and the fluorescence signal intensity.

Figure 3(a) portrays a tomographic image of fluorescence observed with a phantom of light-scattering gel that contains a single fluorescent region in the center. A round shape of the fluorescence image is determined. Some correspondence is apparent: the area of higher signal intensity on the image indicates the embedded area of the localized fluorescent region in the phantom. Periodic changes of signal intensity that appeared along the Y axis are inferred to result from the presence of a standing wave formed in the phantom on the axis of the ultrasound beam. The profile of the signal intensity along the X axis on the image sectioned at the center of the phantom including the fluorescent region is shown in Fig. 3(b). The full width at halfmaximum of the profile is approximately 3 mm, corresponding to the diameter of the embedded fluorescent region. Considering the 3 mm beam diameter of a focused ultrasound field, the spatial resolution observed in the image is appropriate. A photograph of the phantom sectioned in the longitudinal plane is indicated in Fig. 3(c) with a dashed line of the scanned plane. Figure 4 depicts the observed result using a phantom that includes two fluorescent regions with an embedded 9 mm gap along the X axis. Both the image [Fig. 4(a)] and the X-axis profile [Fig. 4(b)] show the two well-separated fluorescence peaks, which

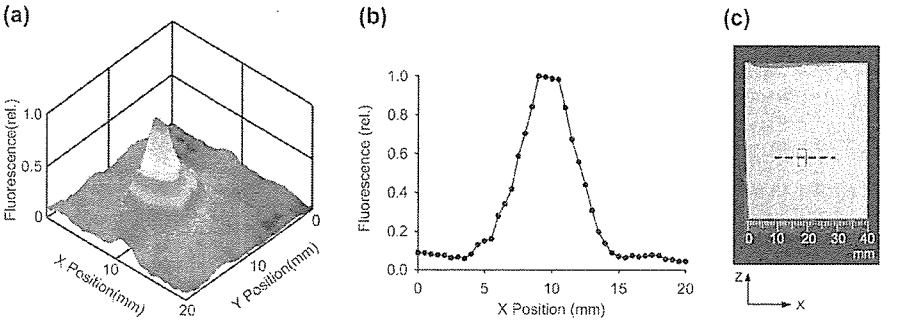

FIG. 3. (Color online) (a) Tomographic image of fluorescence observed with a phantom of light-scattering gel with a single fluorescent region in the phantom's center. (b) Profile of the signal intensity along with X axis on the image sectioned at the center of the phantom, which contains the embedded fluorescent region. (c) Photograph sectioned in the longitudinal plane of the phantom. An embedded fluorescent region is outlined. A dashed line shows the scanning plane of measurement.

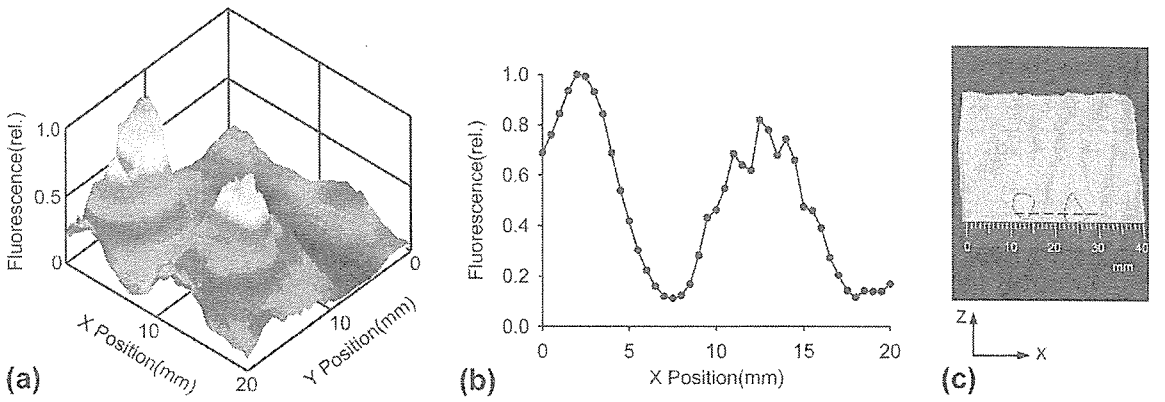

FIG. 4. (Color online) (a) Tomographic image of fluorescence observed with a phantom; the phantom was made of light-scattering gel with two fluorescent regions and a 9 mm gap. (b) Profile of the signal intensity along the *X* axis on the image sectioned at the center of the phantom, which contains the embedded fluorescent regions. (c) Photograph sectioned in the longitudinal plane of the phantom. Two embedded fluorescent regions are outlined. A dashed line shows the scanning plane of measurement.

correspond to the embedded positions of both regions, as shown in the photograph sectioned on the longitudinal plane of the phantom [Fig. 4(c)]. Taking into consideration the reduced scattering coefficient of the phantom, which is estimated as 0.61 mm^{-1} at the measured wavelength, this technique is potentially applicable for biological tissues. It can be used to obtain a tomographic image of fluorescence using near-infrared light. Although a quantitative comparison is necessary to apply this technique for absolute measurements of the distribution of fluorescence intensity, the results obtained here suggest that this simple method is potentially useful for imaging to resolve the position of a localized fluorescent region in a scattering medium. Considering this, further progress in the development of scanning techniques based on an array transducer can provide a method for measuring fluorescence buried in scattering media such as biological tissues. This technique is expected to facilitate the expansion of fluorescent probes' use for biological applications throughout the fields of life science and medicine.

This work was supported in part by grants from the Japanese Ministry of Education, Culture, Sports, Science, and Technology, from Innovation Plaza Miyagi, the Japan Science and Technology Agency, and from the Tohoku Institute of Technology.

[1]E. M. Sevick-Muraca, E. Kuwana, A. Godavarty, J. P. Houston, A. B. Thompson, and R. Roy, in *Biomedical Photonics Handbook*, edited by T. Vo-Dinh (CRC, Boca Raton, FL, 2003), 33, pp. 1.
[2]M. Toida, M. Kondo, T. Ichimura, and H. Inaba, Appl. Phys. B: Photophys. Laser Chem. **52**, 391 (1991).
[3]B. Devaraj, M. Takeda, M. Kobayashi, M. Usa, K. P. Chan, Y. Watanabe, T. Yuasa, T. Akatsuka, M. Yamada, and H. Inaba, Appl. Phys. Lett. **69**, 3671 (1996).
[4]M. Kempe, M. Larionov, D. Zaslavsky, and Z. Genack, J. Opt. Soc. Am. A **14**, 1151 (1997).
[5]G. D. Mahan, W. E. Engler, J. J. Tiemann, and E. Uzgiris, Proc. Natl. Acad. Sci. U.S.A. **95**, 14015 (1998).
[6]L. V. Wang, S. L. Jacques, and X. Zhao, Opt. Lett. **20**, 629 (1995).
[7]L. V. Wang, Phys. Rev. Lett. **87**, 043903 (2001).

Available online at www.sciencedirect.com
ScienceDirect
Biochemical and Biophysical Research Communications 351 (2006) 7–13
BBRC
www.elsevier.com/locate/ybbrc

Reduction in nonfluorescence state of quantum dots on an immunofluorescence staining

Songhua Li-Shishido [a], Tomonobu M. Watanabe [b], Hiroshi Tada [a], Hideo Higuchi [b,*], Noriaki Ohuchi [a]

[a] *Division of Surgical Oncology, Graduate School of Medicine, Tohoku University, Japan*
[b] *Biomedical Engineering Research Organization, Tohoku University, Japan.*

Received 8 September 2006
Available online 9 October 2006

Abstract

Fluorescence quantum dots are widely used in immunofluorescence staining because of their intense and stable fluorescence. However, the nonfluorescence state of the quantum dots is their disadvantage. Here, the nonfluorescence state of the dots labeled to cells and tissues was suppressed. Cells and tissues where the receptor HER2 had been overexpressed were fixed and then labeled with anti-HER2 cross-linked with the dots. The intensity of the dots increased with the illumination time. The majority of the single dots were in the nonfluorescence state at beginning of the illumination period and the number of fluorescence dots observed increased with the illumination time. Living cells were also labeled with the anti-HER2-Qdots. Blinking and bleaching of the Qdots was effectively suppressed by adding β-mercaptoethanol and glutathione. Therefore, the movement of the Qdots bound to cell membrane could be observed for long periods of time.

Keywords: Quantum dots; Immunofluorescence; Fixed cell; Fixed tissue; Live cell; Imaging; Single particles; Single molecules; Nanotechnology

The fluorescence quantum dots (Qdots) are nanocrystals of semiconductor materials, for example, CdSe and CdTe [1–4]. The wavelength of the fluorescence of the Qdots changes with the diameter of the crystals. Small sized crystals (~2 nm in diameter of CdSe) emit blue fluorescence and larger crystals (~4 nm) emit red fluorescence [1]. The quantum yield of fluorescence emission is affected by the environmental conditions [5]. To get higher quantum yield of fluorescence, the Qdots were coated with the other semiconductor, for example, ZnS [5]. For use in biological experiments, the Qdots were coated further with a polymer which has reactive sites, amine or carboxyl groups, to conjugate with proteins, DNA and RNA [6]. After conjugation, the Qdots are imaged to determine the localization of target biological molecules and measure the number of target molecules [7–9].

The fluorescence intensity of the Qdots is considerably higher than that of organic dyes. They do not bleach for long period of time even in the absence of anti-fading reagents, which would destroy cell [8]. These advantages of the Qdots have been widely used in the biological and medical fields [3,10]. The disadvantage of the Qdots is that they bind reversibly to a nonfluorescence state which results in blinking and low fluorescence intensity [11–13]. To measure the number or intensity of the Qdots that have bound to cells, the intensity of each Qdot must be stable. To observe single Qdots labeled to proteins for long periods of time, the Qdots must emit fluorescence for long periods without blinking [13,14].

In this study, the nonfluorescence state (off-state) of the antibody–Qdot complex bound to the cells was reduced in order to improve the quantitative measurements and fluorescence period of the Qdots. The period at fluorescence

* Corresponding author. Fax: +81 22 795 5753.
E-mail address: higuchi@tubero.tohoku.ac.jp (H. Higuchi).

0006-291X/S - see front matter © 2006 Elsevier Inc. All rights reserved.
doi:10.1016/j.bbrc.2006.09.159

state (on-state) of the Qdots bound to fixed and embedded cells increased with the time when that were illuminated by laser. The reducing agents, β-mercaptoethanol or glutathione, were inhibited the off-state.

Materials and methods

Qdot was conjugated to chimeric monoclonal antibody against HER2, trastuzumab (Herceptin, Chugai Pharmaceutical Ltd.) with Qdots 605, 655, and 705, where the number indicates the wavelength at maximum fluorescence. An antibody Conjugation Kit (Qdot corporation) was used [7,15] according to the manufacturer's instructions. The final concentration of trastuzumab–Qdots was determined by measuring the conjugate absorbance.

The human breast cancer cell line KPL-4, which overexpresses HER2 and is sensitive to trastuzumab [16,17], was kindly provided by Dr. J. Kurebayashi. KPL-4 cells were cultured in DMEM supplemented with 5% fetal bovine serum. MDA-MB-231 cells having a low expression of HER2 were maintained in L-15 medium, respectively, with 10% fetal bovine serum [16,18,19].

A suspension of KPL-4 cells was transplanted subcutaneously to the dorsal skin of female Balb/c nu/nu mice at ~5 weeks of age (Charles River). Several weeks after tumor inoculation, mice bearing a tumor with a volume of 100–200 mm^3 were selected. The mice were sacrificed with an overdose of CO_2. The tumors were removed and divided. All operations on animals were in accordance with the institutional animal use and care regulations.

For the immuno histochemical analysis, cells on a coverslip were fixed at 10% neutral-buffered formalin for 10 min [8]. Fixed cells were extensively washed three times with PBS solution. To minimize the nonspecific binding of trastuzumab-Q dot complexes to the cells, the cells were treated with the blocking solution containing NH_4Cl, glycine, FBS or BSA. The best treatment for blocking was incubating the cells in PBS solution containing 50 mM NH_4Cl for 10 min and then in 10% FBS for 30 min after a through washing with NH_4Cl.

The trastuzumab–Qdot complexes or polyclonal anti-HER2 cells from rabbit were reacted with the cells that had been blocked. The anti-HER2 cells were further reacted with anti-rabbit IgG conjugated with Qdots.

Tumors were fixed in 10% neutral-buffered formalin overnight [8] and then transferred into ethanol before processing and paraffin embedding. The tissue after removing paraffin was then treated with the PBS solution containing trastuzumab–Qdots. The fixed cells and tissue were embedded into Permafluor™ (Thermo Shandon).

Qdots were observed under microscopes (IX71 or BX51, Olympus) [20,21], equipped with green laser (532 nm), long pass filter (>580 nm). Fixed cells were observed at a power density of 11 (Fig. 1), or 31 W/mm^2 (Figs. 2–4). The x- and y-positions of the fluorescent spot were calculated by fitting the data to a 2D-Gaussian curve [21].

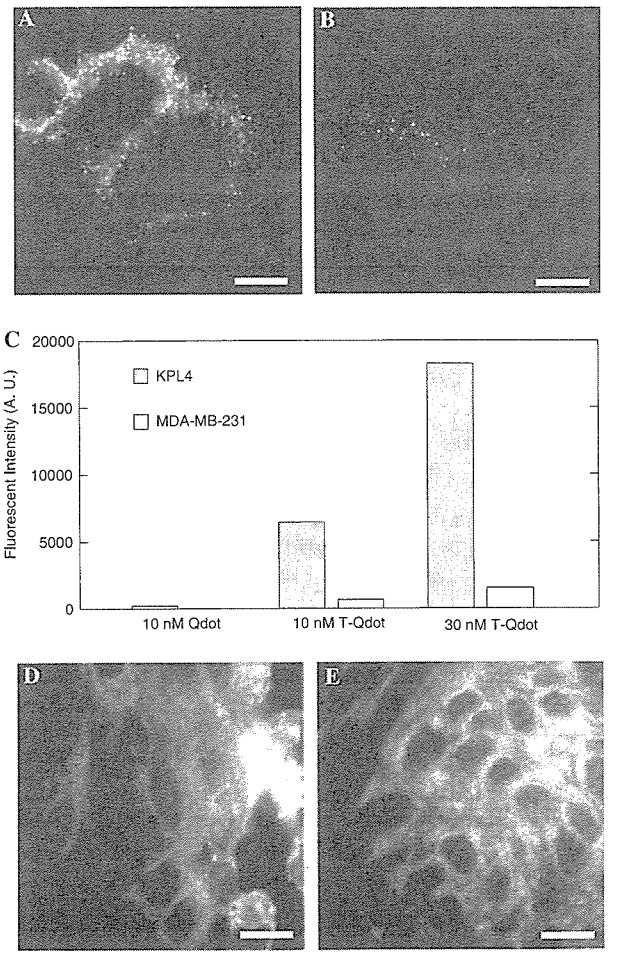

Fig. 1. Antibody–Quantum dot complex bound to cells and the tumor. Qdot705 (30 nM) labeled with trastuzumab bound to fixed KPL-4 cells (A) and MDA-MB-231 cells (B). (C) Fluorescence intensity of Qdots measured in several different cells. Open and closed bars indicate the intensity of KPL-4 and MDA-MB-231 cells, respectively. The two bars on the left-hand side show Qdots that have not bound trastuzumab after they had been mixed with the cells. Bars in the center and on the right show results in the presence of trastuzumab. (D) Sections of a tumor in a mouse, 5 μm thickness, were stained using Qdot-705 (10 nM) and labeled with trastuzumab. (E) The section was reacted with rabbit anti-HER2 and then with Qdot-705 (10 nM) labeled with anti-rabbit IgG. Scale bars = 10 μm (A, B, D, and E). Images were taken at an exposure time of 0.2 s at laser power of 11 W/mm^2.

Results

The trastuzumab–Qdots bound well to KPL-4 cells but not to the MDA-MB-231 cells which expressed HER2 at low levels [19] (Fig. 1A and B). Most of the Qdots bound to the cell membrane (Fig. 1A). The intensity of the Qdots bound to the cells was measured in order to estimate the number of the bound Qdots. The Qdots without trastuzumab labeling did not bind to KPL-4 and MDA-MB-231 cells (Fig. 1C). The intensity of the Qdots bound to KPL-4 was approximately 10 times higher than those bound to MDA-MB-231 cells. This result was consistent with the expression of HER2 in these cells [19].

The trastuzumab–Qdots were bound to a tumor transplanted in a nude mouse. The trastuzumab–Qdots bound mainly to the region near the KPL-4 cell membrane (Fig. 1D). The tumor also reacted with the polyclonal anti-HER2 cells from rabbits and then with anti-rabbit IgG labeled with the Qdots (Fig. 1E). The rabbit-IgG–Qdots bound to the cell membrane in similar areas where the trastuzumab–Qdots bound using direct staining methods (Fig. 1D and E). These results indicate that the fixed cells and tumor cells could be successively stained with antibodies labeled with the Qdots.

The change in fluorescence intensity of the antibody–Qdots was measured after illuminating the sections for long periods by a laser to test the stability of fluorescence emis-

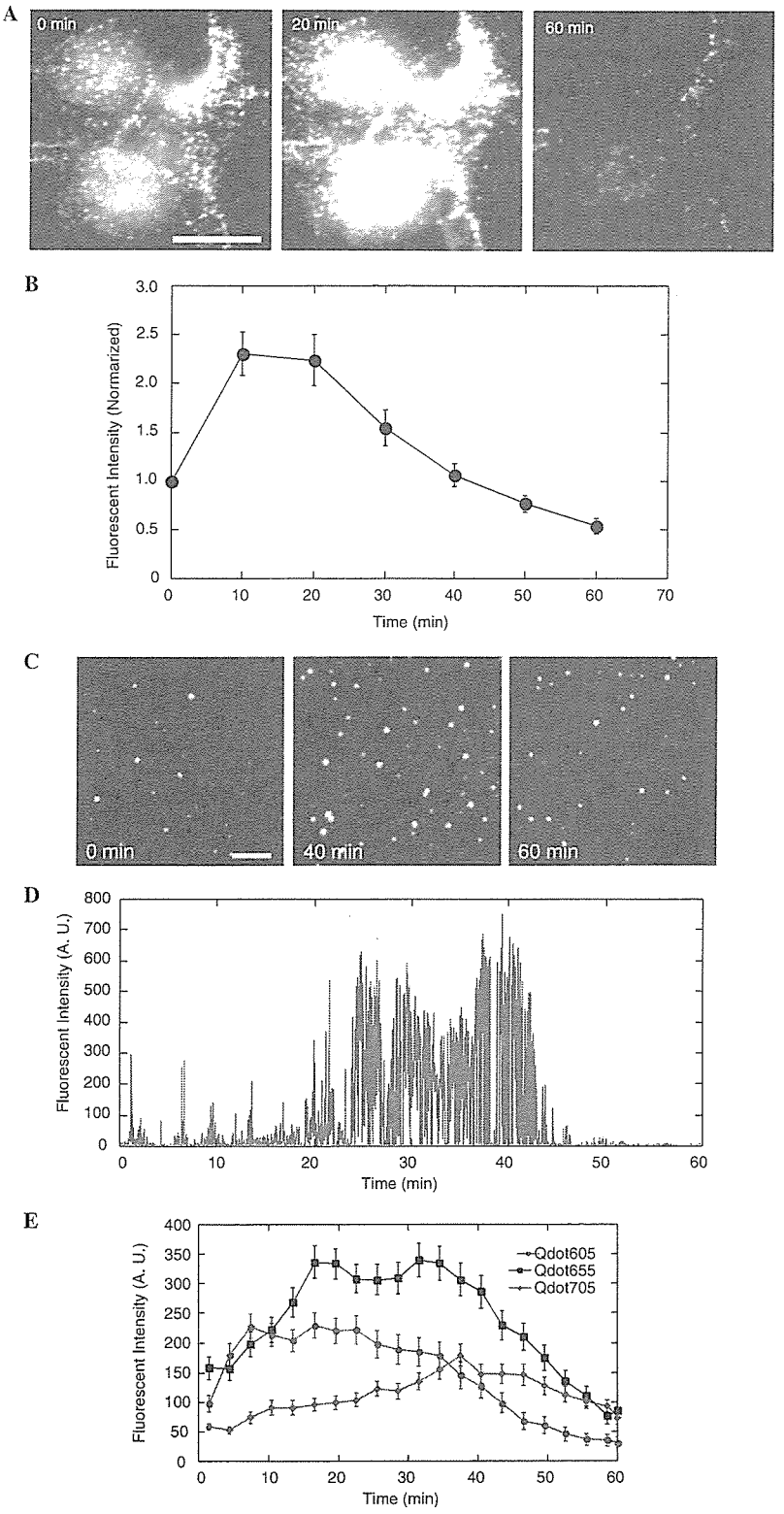

Fig. 2. Change in Qdot intensity when illuminated by a green laser. KPL-4 cells were labeled with trastuzumab–Qdot-705 (10 nM). Qdots were illuminated by the green laser at a laser power of 74 W/mm^2. (A) Images were taken at an exposure time of 0.05 s at illumination periods of 0, 20, and 60 min. Scale bar indicates 10 μm. (B) Intensity in several regions were measured. (C) Trastuzumab–Qdots-705 (0.1 nM) were spread on a coverslip. Images were taken at exposures time of 1 s at illumination periods of 0, 40, and 60 min using a laser power of 74 W/mm^2. Scale bar = 10 μm. (D) Intensity at several regions was measured at an exposure time of 1 s. (E) The average of hundreds of intensities from Qdots-605 (red symbols), 655 (blue), and 705 (green).

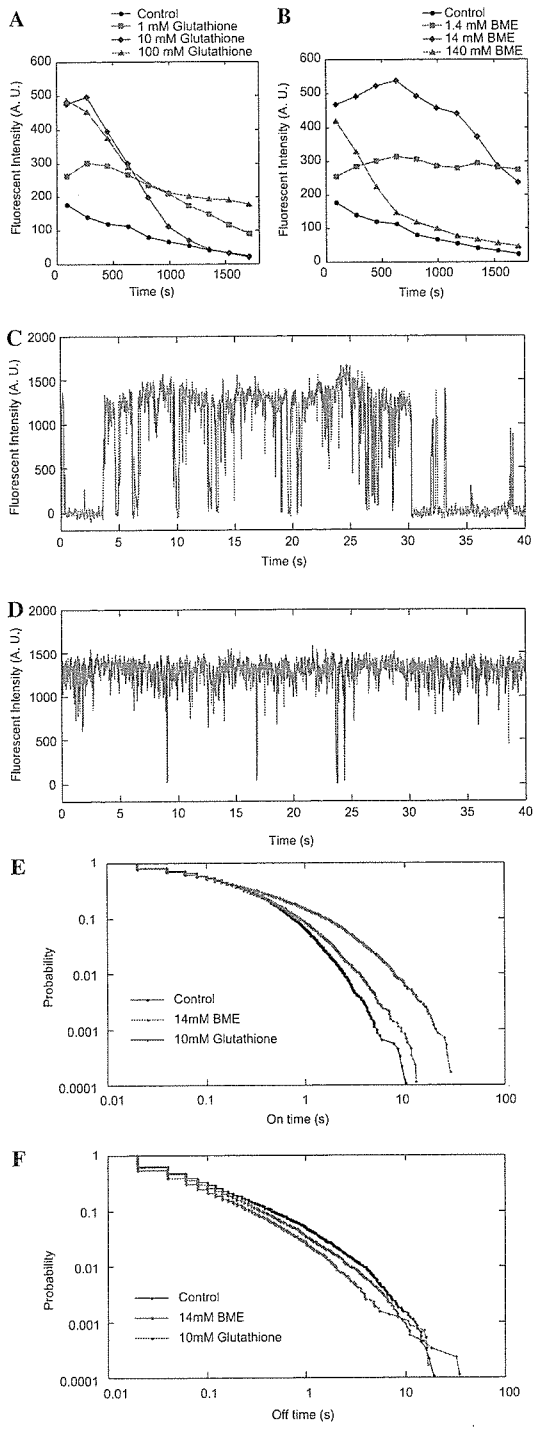

Fig. 3. The on- and off-dwell times in the presence of reducing agents. Qdot-655 (0.1 nM) in PBS solution containing BME (0, 1.4, 14, and 140 mM, (A)) and glutathione (0, 1, 10, and 100 mM, (B)) were spread on coverslips. Images were taken at exposure time of 1 s for 30 min at a laser power of 74 W/mm^2. (C,D) Images in the absence (C) and presence (D) of 14 mM BME were taken at beginning of the illumination period at exposure times of 20 ms and a laser power of 74 W/mm^2. (E,F) Fluorescence of the on- and off- dwell times was measured from the results shown in (C) and (D). The total dwell time was calculated from the probability.

sion. The power of green laser was increased by ~ 7 times to accelerate the intensity change. The intensity increased prominently 20 min into the illumination period (Fig. 2A). Sixty minutes into the illumination period, the intensity had returned to its original levels. The intensities at many regions in cells could be quantitatively analyzed relative to the initial intensity (Fig. 2B). In contrast, the fluorescence intensity of an organic fluorescence molecule, Cy3, conjugated to trastuzumab decreased exponentially with the illumination time (data not shown). The time constant was only 20 s.

To find the reason for this enhancement of intensity, the intensity of single Qdots embedded into Permafluor™ without being attached to cells was analyzed. Sequential images were taken every 1 s (Fig. 2C). The number of fluorescence Qdots appeared to increase, while the intensity of the bright Qdots changed little (Fig. 2C). Fig. 2D shows the intensity change in relation to the illumination time. The intensity of most Qdots increased firstly and decreased with time. During the periods where the Qdots exhibited their highest intensity, i.e., 20–43 min after the start of the illumination period (Fig. 2D), Qdots blinked from zero to maximum intensity. Assemble averages of the intensity of Qdot-705 showed that the intensity increased at the beginning and then gradually decreased to the end (Fig. 2E). The other Qdots, 605 and 705, showed similar intensity profiles to the Qdot-655 but had different time constants.

Fluorescence imaging is also used for position measurements of proteins [21,22]. To observe the position of Qdots bound to living cells, we determined the most suitable conditions that allowed Qdots to bind for long periods of time with high spatial and temporal precision [21]. The reducing reagent, DTT and β-mercaptoethanol (BME), are known to suppress the blinking but its effects on the bleaching time have not been determined [13]. We investigated the effect of BME and glutathione on both the bleaching and blinking. The intensity increased several fold in the presence of the reducing agents comparing to that in the absence (Fig. 3A and B). The intensity decreased with the time illuminated by the laser. The intensity in the presence of 1 and 100 mM glutathione, 1.4 and 14 mM BME suppressed the reduction of intensity for long time (30 min). In the presence of 10 mM glutathione and 140 mM BME, the intensity was reduced only at the beginning (<20 min) and not thereafter.

To analyze the blinking of the fluorescence intensity, the temporal resolution of the imaging was improved to be 20 ms (Fig. 3C and D). In the absence of the reducing agent, the Qdots blinked frequently and showed long dwell times in the off-state. In the presence of BME, the Qdots emitted the fluorescence continuously for long periods of time without spending long periods in the off-state. To evaluate the suppression of blinking, the dwell times of on and off-states were analyzed [13]. The probability of Qdots being in the state of long on-dwell time in the presence of BME is much higher than that in the absence of BME. For example, the probabilities of Qdots having on-

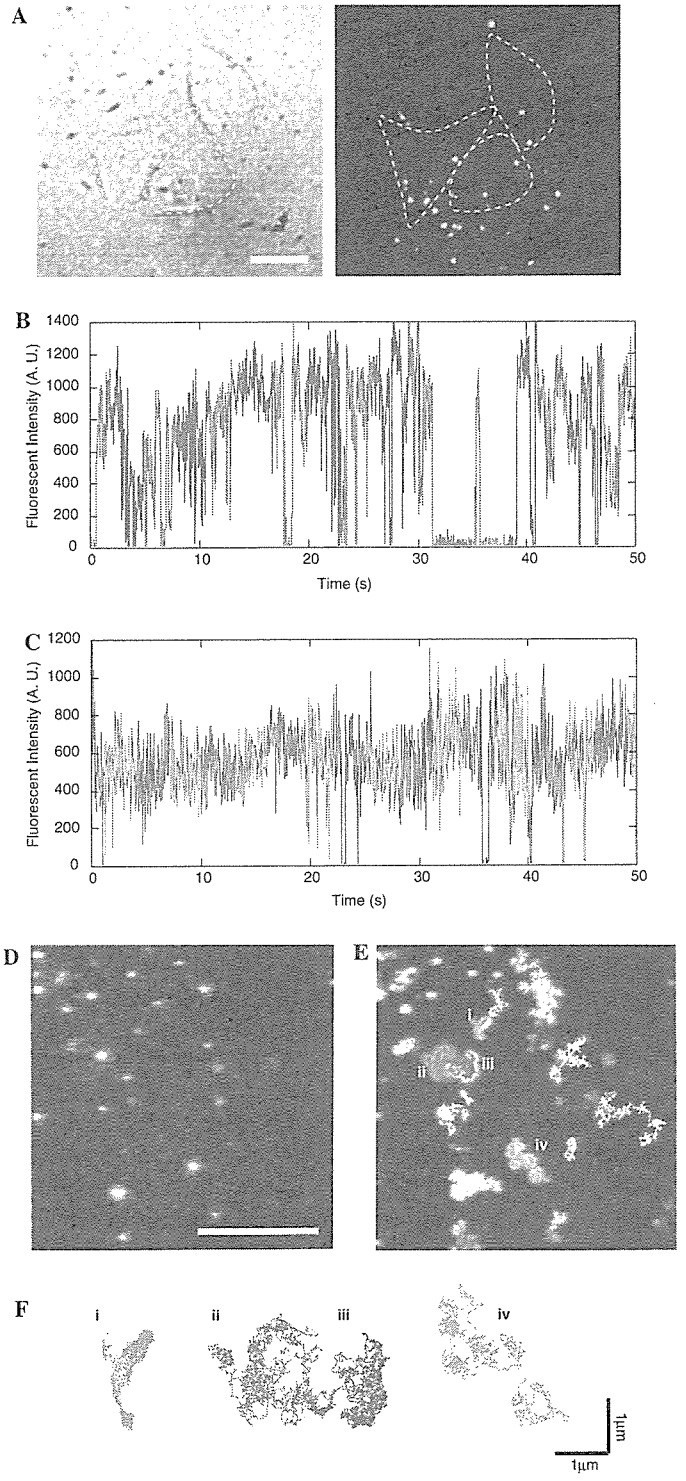

Fig. 4. Blinking of Qdots bound to living cells. Qdots-655 (0.5 nM) labeled with trastuzumab were bound to living KPL-4 cells. (A) There are a bright field (left) and fluorescence (right) images of the cells. Dotted lines indicate the edge of the cells. Scale bar = 10 μm. The blinking of Qdots in the absence (B) and presence (C) of 14 mM BME is shown at an exposure time of 20 ms. (D) Fluorescence images of Qdots were taken under a total internal reflection microscope at an exposure time of 20 ms and laser power of ~70 W/mm^2. Scale bar = 5 μm. (E) The Qdots bound to cells were taken at a higher magnification. To trace the movement of Qdtos, 2500 images were collected over a 50 s period and then superimposed. Colored lines indicate the traces of single Qdots. (F) Traces indicate movements of Qdots that occurred on the cell membrane for a 50 s period.

dwell times of 5 s are approximately 2.3% in the presence of BME which are considerably higher than 0.10% in the absence of BME. The off-dwell time is also higher in the absence of BME. Long on-dwell times and short off-dwell times observed in the presence of BME indicate that the Qdots stay in the on-state for most of the time.

The imaging of proteins in living cells is an important application of Qdots. The trastuzumab–Qdot complexes were mixed with living cells to detect the movement of membrane receptor, HER2, in the presence of BME. The movement of the Qdots was measured within the first 30 min when the activity of the cells was not altered.

The trastuzumab–Qdot complexes bound to the membrane of the cells (Fig. 4A). Qdots in the absence of BME often exhibited blinking (Fig. 4B). Most on-dwell times were less than 1 s. The long off-dwell times were common. In the presence of 14 mM BME, the on-dwell times became longer than 1 s for many of the Qdots (Fig. 4C). The off-dwell time was very short <0.2 s (Fig. 4C).

The position of the Qdots bound to cell membrane was measured by fitting the data of the fluorescence of the spots to two-dimensional Gaussian with one nanometer precision [21,23]. Fig. 4D shows the initial image of the Qdots bound to the cell membrane. All images have been superimposed as shown in Fig. 4E. The center of the fluorescence spots was measured continuously for 50 s without losing the data by off-dwell (colored traces in Fig. 4E). Traces on an expanded time scale show the detailed movement of the Qdots (Fig. 4F). Most of the Qdots moved a distance of 3 μm in 50 s which is considerably shorter than that of free diffusion of trastuzumab–Qdots (~30 μm assuming the diameter of 30 nm). The some of movements of the Qdots were random (Fig. 4F(i and ii)). Some of the Qdots moved within a narrow area (iii). Other Qdots moved within small area and then hoped to the next area (iv).

Discussion

The intensity of the Qdots bound to KPL-4 cells was approximately 10 times higher than that to MDA-MB-231 cells. This result is consistent with the expression HER2 in these cells [16,18,19]. The advantage of Qdot immunofluorescence staining is that quantitative analysis of bound Qdots to cells is possible. Another advantage is the higher sensitivity as even single Qdots can be imaged (Figs. 2C and 4D) [13,14,21]. The trastuzumab–Qdots also bound selectively to a tumor formed by KPL-4 cells transplanted in a nude mouse, suggesting this technique has applications for medical immunohistochemistry [3,24,25].

Organic fluorescent dyes for immunofluorescence staining are not suitable for quantitative analysis because of their low intensity and rapid bleaching within 20 s of illumination [8]. The trastuzumab–Qdots remained stable for periods up to 1 h (Fig. 2) [8,13,26,27]. The intensity of the Qdots did not change much in the first ~10 min after laser illumination (Fig. 2E). The intensity then gradually increased to 2–3 times of from the initial intensity and then decreased [26]. These changes in intensity were also obtained for Qdots labeled cells stored in the Permafluor for 3 months at room temperature (data not shown). These results indicate that Qdots are very useful for quantitative analysis of immunofluorescence staining even when they have been stored for long periods.

Measurements of the intensity of single Qdots indicated that the number of Qdots at the fluorescence on-state increases with time (Fig. 2). The single Qdots were bleached by long-term continuous illumination with a laser. These changes in intensity of single Qdots explain the change in intensity of multiplied Qdots bound to cells (Fig. 2). Single Qdots analysis is a powerful method to determine the fundamental properties of Qdots [14,21].

The reducing agents, BME and DTT, suppressed the blinking of intensity of Qdots [13]. The intensity of Qdots in the presence of BME and glutathione was measured. BME (1.4 mM or higher) and glutathione (1 mM or higher) considerably enhanced the on-dwell time and shortened the off-dwell time marginally. The on-dwell time was enhanced in the presence of 14 mM BME but not in the presence of 140 mM BME. The enhancement of on-dwell time by the reducing agents was consistent with the previous results [13].

The longer on-dwell times and shorter off-dwell times increased the possibility that Qdots would stay in the on-state (Fig. 3C–F). Therefore, the total intensity of Qdots increased considerably at the beginning of the illumination period (Fig. 3A and B). Illumination for long periods using a laser resulted in the Qdots bleaching and the total intensity gradually decreasing. The decay time of the intensity by photobleaching was slowest in the presence of 14 mM BME. At higher concentrations of BME (140 and 280 mM), the intensity decay time was shorter. The optimum conditions for suppressing the bleaching and blinking were 14 mM BME.

Qdots bind to proteins in both *in vitro* motility assays and in cells [14,21]. The higher intensity of the fluorescence has made it possible to precisely detect the position of Qdot within a few nanometers and milliseconds. Because many of Qdots did not exhibit the blinking for >10 s, the Qdot position was measured for long time without missing the data by blinking (Fig. 4D–F). The movements of Qdots are much slower than that at free diffusion. Some of Qdots showed the hopping movement from the one area to the other, which is consistent with previous reports [28].

Stable and intense fluorescence of Qdots are advantageous for fluorescence imaging. However, blinking and non-specific binding of Qdots must be acknowledged as potential problems. Here non-specific binding was avoided by the improvement of blocking method. The off-state of Qdots bound to fixed and embedded cells was suppressed by the illumination of laser. The blinking of Qdots bound to living cells were suppressed effectively in the presence of 14 mM BME. These improvements open-up the new applications of Qdots such as medical immunostaining and nanometer measurement of position.

Acknowledgments

We thank Ms. Sachiko Higuchi and Dr. J.M. West for helping. This work was supported by Grants-in-Aid for Research Project, Promotion of Advanced Medical Technology (N.O.), Scientific Research in Priority Areas from the Japan MEXT (H.H.), and Special Coordination Funds for Promoting Science and Technology of Japan (H.H., T.M., and N.O.).

References

[1] M. Bruchez Jr., M. Moronne, P. Gin, S. Weiss, A.P. Alivisatos, Semiconductor nanocrystals as fluorescent biological labels, Science 281 (1998) 2013–2016.
[2] W.C. Chan, S. Nie, Quantum dot bioconjugates for ultrasensitive nonisotopic detection, Science 281 (1998) 2016–2018.
[3] X. Gao, Y. Cui, R.M. Levenson, L.W. Chung, S. Nie, In vivo cancer targeting and imaging with semiconductor quantum dots, Nat. Biotechnol. 22 (2004) 969–976.
[4] X. Michalet, F.F. Pinaud, L.A. Bentolila, J.M. Tsay, S. Doose, J.J. Li, G. Sundaresan, A.M. Wu, S.S. Gambhir, S. Weiss, Quantum dots for live cells, in vivo imaging, and diagnostics, Science 307 (2005) 538–544.
[5] X. Peng, M.C. Schlamp, A.V. Kadavanich, A.P. Alivisatos, Epitaxial growth of highly luminescent CdSe/CdS core/shell nanocrystals with photostability and electronic accessibility, J. Am. Chem. Soc. 119 (1997) 7019–7029.
[6] W.C. Chan, D.J. Maxwell, X. Gao, R.E. Bailey, M. Han, S. Nie, Luminescent quantum dots for multiplexed biological detection and imaging, Curr. Opin. Biotechnol. 13 (2002) 40–46.
[7] I.L. Medintz, H.T. Uyeda, E.R. Goldman, H. Mattoussi, Quantum dot bioconjugates for imaging, labeling and sensing, Nat. Mat. 4 (2005) 435–446.
[8] X. Wu, H. Liu, J. Liu, K.N. Haley, J.A. Treadway, J.P. Larson, N. Ge, F. Peale, M.P. Bruchez, Immunofluorescent labeling of cancer marker Her2 and other cellular targets with semiconductor quantum dots, Nat. Biotechnol. 21 (2003) 41–46.
[9] D.S. Lidke, P. Nagy, R. Heintzmann, D.J. Arndt-Jovin, J.N. Post, H.E. Grecco, E.A. Jares-Erijman, T.M. Jovin, Quantum dot ligands provide new insights into erbB/HER receptor-mediated signal transduction, Nat. Biotechnol. 22 (2004) 198–203.
[10] B.N. Giepmans, T.J. Deerinck, B.L. Smarr, Y.Z. Jones, M.H. Ellisman, Correlated light and electron microscopic imaging of multiple endogenous proteins using Quantum dots, Nat. Methods 2 (2005) 743–749.
[11] M. Nirmal, B.O. Dabbousi, M.G. Bawendi, J.J. Macklin, J.K. Trautman, T.D. Harris, L.E. Brus, Fluorescence intermittency in single cadmium selenide nanocrystals, Nature 383 (1996) 802–804.
[12] G. Schlegel, J. Bohnenberger, I. Potapova, A. Mews, Fluorescence decay time of single semiconductor nanocrystals, Phys. Rev. Lett. 88 (2002) 137401.
[13] S. Hohng, T. Ha, Near-complete suppression of quantum dot blinking in ambient conditions, J. Am. Chem. Soc. 126 (2004) 1324–1325.
[14] D.M. Warshaw, G.G. Kennedy, S.S. Work, E.B. Krementsova, S. Beck, K.M. Trybus, Differential labeling of myosin V heads with quantum dots allows direct visualization of hand-over-hand processivity, Biophys. J. 88 (2005) L30–L32.
[15] X. Gao, L. Yang, J.A. Petros, F.F. Marshall, J.W. Simons, S. Nie, In vivo molecular and cellular imaging with quantum dots, Curr. Opin. Biotechnol. 16 (2005) 63–72.
[16] J. Kurebayashi, T. Otsuki, C.K. Tang, M. Kurosumi, S. Yamamoto, K. Tanaka, M. Mochizuki, H. Nakamura, H. Sonoo, Isolation and characterization of a new human breast cancer cell line, KPL-4, expressing the Erb B family receptors and interleukin-6, Br. J. Cancer 79 (1999) 707–717.
[17] J. Kurebayashi, Regulation of interleukin-6 secretion from breast cancer cells and its clinical implications, Breast Cancer 7 (2000) 124–129.
[18] H. Kunisue, J. Kurebayashi, T. Otsuki, C.K. Tang, M. Kurosumi, S. Yamamoto, K. Tanaka, H. Doihara, N. Shimizu, H. Sonoo, Anti-HER2 antibody enhances the growth inhibitory effect of anti-oestrogen on breast cancer cells expressing both oestrogen receptors and HER2, Br. J. Cancer 82 (2000) 46–51.
[19] K. Fujimoto-Ouchi, F. Sekiguchi, Y. Tanaka, Antitumor activity of combinations of anti-HER-2 antibody trastuzumab and oral fluoropyrimidines capecitabine/5′-dFUrd in human breast cancer models, Cancer Chemother. Pharmacol. 49 (2002) 211–216.
[20] V.T. Nguyen, Y. Kamio, H. Higuchi, Single-molecule imaging of cooperative assembly of gamma-hemolysin on erythrocyte membranes, EMBO J. 22 (2003) 4968–4979.
[21] S. Toba, T.M. Watanabe, L. Yamaguchi-Okimoto, Y.Y. Toyoshima, H. Higuchi, Overlapping hand-over-hand mechanism of single molecular motility of cytoplasmic dynein, Proc. Natl. Acad. Sci. USA 103 (2006) 5741–5745.
[22] M. Ueda, Y. Sako, T. Tanaka, P. Devreotes, T. Yanagida, Single-molecule analysis of chemotactic signaling in dictyostelium cells, Science 294 (2001) 864–867.
[23] A. Yildiz, J.N. Forkey, S.A. McKinney, T. Ha, Y.E. Goldman, P.R. Selvin, Myosin V walks hand-over-hand: single fluorophore imaging with 1.5-nm localization, Science 300 (2003) 2061–2065.
[24] S. Kim, Y.T. Lim, E.G. Soltesz, A.M. De Grand, J. Lee, A. Nakayama, J.A. Parker, T. Mihaljevic, R.G. Laurence, D.M. Dor, L.H. Cohn, M.G. Bawendi, J.V. Frangioni, Near-infrared fluorescent type II quantum dots for sentinel lymph node mapping, Nat. Biotechnol. 22 (2004) 93–97.
[25] N.Y. Morgan, S. English, W. Chen, V. Chernomordik, A. Russo, P.D. Smith, A. Gandjbakhche, Real time in vivo non-invasive optical imaging using near-infrared fluorescent quantum dots, Acad. Radiol. 12 (2005) 313–323.
[26] Z. Zhelev, R. Jose, T. Nagase, H. Ohba, R. Bakalova, M. Ishikawa, Y. Baba, Enhancement of the photoluminescence of CdSe quantum dots during long-term UV-irradiation: privilege or fault in life science research? J. Photochem. Photobiol. B: Biol. 75 (2004) 99–105.
[27] K. Hanaki, A. Momo, T. Oku, A. Komoto, S. Maenosono, Y. Yamaguchi, K. Yamamoto, Semiconductor quantum dot/albumin complex is a long-life and highly photostable endosome marker, Biochem. Biophys. Res. Commun. 302 (2003) 496–501.
[28] K. Suzuki, K. Ritchi, E. Kajikawa, T. Fujiwara, A. Kusumi, Rapid hop diffusion of a G-protein coupled receptor in the plasma membrane as revealed by single-molecule techniques, Biophys. J. 88 (2005) 3659–3680.

ADVANCED MATERIALS

DOI: 10.1002/adma.200600964

Colloidal Ceria Nanocrystals: A Tailor-Made Crystal Morphology in Supercritical Water**

By *Jing Zhang, Satoshi Ohara, Mitsuo Umetsu, Takashi Naka, Yoshiharu Hatakeyama,* and *Tadafumi Adschiri**

The synthesis of colloidal metal oxide nanocrystals with controlled shape is of fundamental and technological interest because in this way it is possible to tune their shape-dependent physical properties and thus consolidate their promising applications in optics, catalysis, biosensing, and data storage. Recently, the organic-solution phase[1–3] and liquid–solid–solution phase synthetic transfer routes[4] have been demonstrated to be versatile pathways toward such shape-controlled metal oxide nanocrystals. In all of these methods, organic surfactants play a key role in determining the growth and stability of nanocrystals. Combining this concept and the properties of supercritical water (SCW) will lead to a novel approach for the synthesis of metal oxide nanocrystals. For example, SCW is chemically stable and processing with it is environmentally benign;[5] it acts as a unique medium to aid in the spontaneous nucleation and crystallization of metal oxide nanoparticles;[6] and by using organic ligand molecules that are miscible with SCW, crystal growth can be limited and agglomeration can be inhibited in favor of small, well-dispersed particles.[7,8]

As a well-known metal oxide, and because of its novel properties, ceria (CeO_2) has been extensively applied in catalysis, electrochemistry, and optics. For example, ceria nanocrystals have high oxygen-storage capability and act as an important component in three-way catalytic converters to clean up automotive exhausts.[9] To elevate catalytic activity, it is desirable to prepare ceria samples with a high surface area. So far, ceria nanocrystals with spherical, wire, rod, and tadpole shapes have been synthesized.[10] Along with this research, there is another recent trend aimed at tuning the ceria-crystal shape in order to expose reactive crystal planes for high reactivity.[11] Sayle et al. predicted in their theoretical study that the (100) surface is more reactive than (110) or (111) for the CeO_2/YSZ(110) system (where YSZ is yttria-stabilized zirconia).[11a] Yan and co-workers synthesized ceria nanoparticles with various shapes using a hydrothermal method, and experimentally observed that cubic particles (ca. 36 nm) with exposed {100} crystal planes showed the highest oxygen-storage capacity.[11d] Despite these recent advances, it is still a great challenge to synthesize ceria nanocrystals of high quality in terms of uniform size, well-defined crystal shape, and ease of fabrication. Here, we report a simple and rapid approach for producing colloidal ceria nanocrystals on scales of less than 10 nm, with tailor-made ceria crystal planes, using organic-ligand-assisted supercritical water as the medium.

The synthetic strategy is depicted in Figure 1. This strategy depends on: 1) sub-decananometer single-crystal formation in a supercritical hydrothermal process;[6] 2) the miscibility of the organic ligand molecules with high-temperature water, which is due to the lower dielectric constant of the water;[12] and 3) controlled nanocrystal growth from the selective reaction of organic ligand molecules with the specific inorganic crystal surface. Importantly, the use of water, instead of an organic solvent, provides a green chemistry route to nanometer-size building blocks for advanced materials and devices.

The detailed experimental procedures are described in the Experimental section. Crystal structure and morphology of the synthesized ceria nanocrystals were characterized by means of powder X-ray diffraction (XRD), transmission electron microscopy (TEM), and high-resolution transmission electron microscopy (HRTEM). The XRD patterns of the crystals indicated that they had a fluorite cubic structure (see Supporting Information, Fig. S1). TEM images (Fig. 2a) of the ceria nanocrystals with uncapped surfaces showed spherelike shapes with an average diameter of 7 nm, and the nanocrystals were aggregated (Fig. 2a). The single-crystallinity of samples was confirmed by using HRTEM (Fig. 2d). The {111} and {200} facets, with interplanar spacings of 0.32 and 0.27 nm, respectively, were identified on the basis of data from the standard ceria database (Joint Committee for Powder Diffraction Studies (JCPDS) file, No. 34-0394). When decanoic acid (molar ratio to ceria precursor 6:1) was added to the reaction system, the resulting nanocrystals were nanocubes with an average size of 6 nm. They were self assembled with a nearest-neighbor spacing of ca. 2 nm maintained by the decanoic acid capping group (Fig. 2b). The HRTEM image (Fig. 2e) displayed a cross-lattice pattern with a lattice spacing of 0.27 nm, corresponding to the interplanar separation between the {002} or {020} lattice planes of cubic ceria, which implies the synthesis of

[*] Prof. T. Adschiri, J. Zhang, S. Ohara, M. Umetsu, T. Naka, Y. Hatakeyama
Institute of Multidisciplinary Research for Advanced Materials
Tohoku University
Sendai 980-8577 (Japan)
E-mail: ajiri@tagen.tohoku.ac.jp

[**] This work was supported by a Scientific Research Grant from the Ministry of Education, Science, Sports, and Culture of Japan (TA). This research was also partly supported by the Heiwa Nakajima Foundation (TA) and by a Grant-in-Aid for the COE project titled "Giant Molecules and Complex Systems" (2002). Supporting Information is available online from Wiley or from the authors.

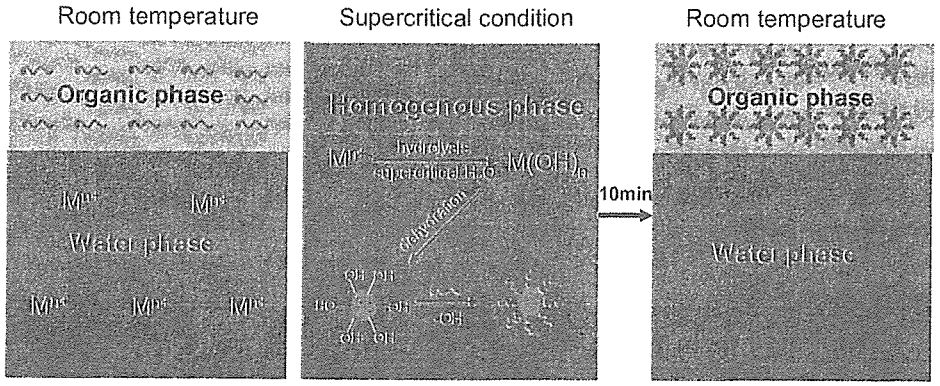

Figure 1. The strategy for the synthesis of metal oxide nanocrystals in the organic-ligand-assisted supercritical hydrothermal process.

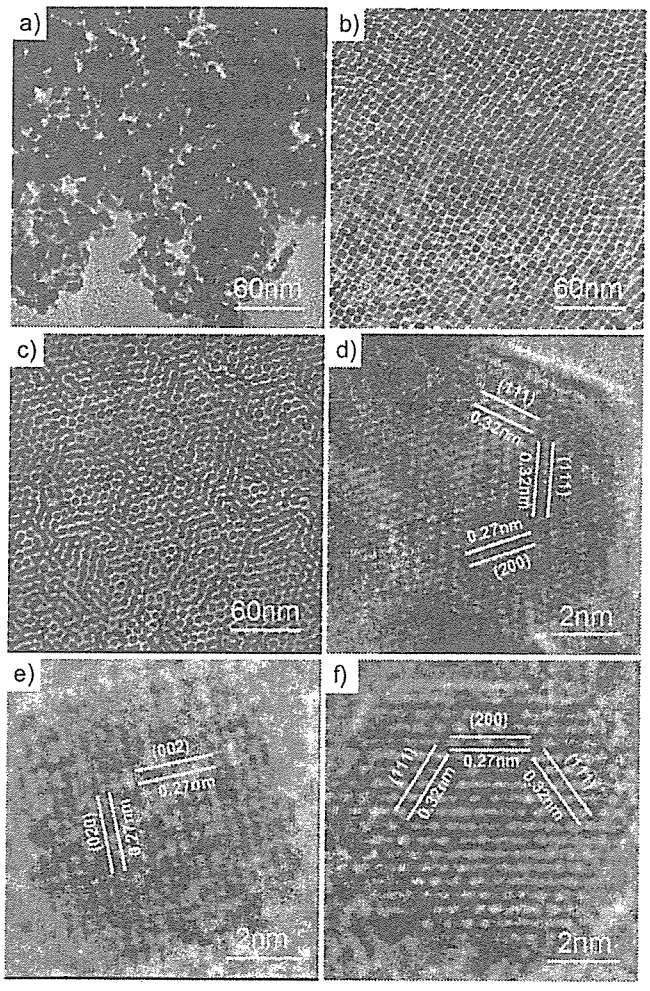

Figure 2. a–c) TEM and d–f) HRTEM images of the synthesized ceria nanocrystals. The molar ratios of decanoic acid to the ceria precursor were 0 (a,d), 6:1 (b,e), and 24:1 (c,f).

ceria nanocubes with (001) surfaces. The exposure of the $CeO_2(001)$ surface was somewhat surprising because this surface is less stable than $CeO_2(111)$. However, it is the most important as it is likely to be the most reactive for catalysis.[11]

For the face-centered cubic (fcc) ceria crystal, as illustrated by Wang and Feng,[13] the shape of the nanocrystals is mainly determined by the ratio (R) between the growth rates along the [100] and [111] directions. By using HRTEM analysis, they found, for particles with an uncapped surface and a size range of 3–10 nm, that the particle shape was dominated by the truncated octahedron that was defined by the (100) and (111) facets. In this experiment, organic ligand molecules had a pronounced effect on the morphology of the nanocrystals formed in the supercritical hydrothermal process, as described in Figure 3. The shape of the naked ceria nanocrystals with an average diameter of 7 nm was the {200}- and {111}-enclosed truncated octahedron, which is similar to the results of Wang and Feng.[13] When the decanoic acid (molar ratio to ceria precursor 6:1) was introduced into the supercritical hydrothermal reaction, the organic ligand molecules were miscible with water

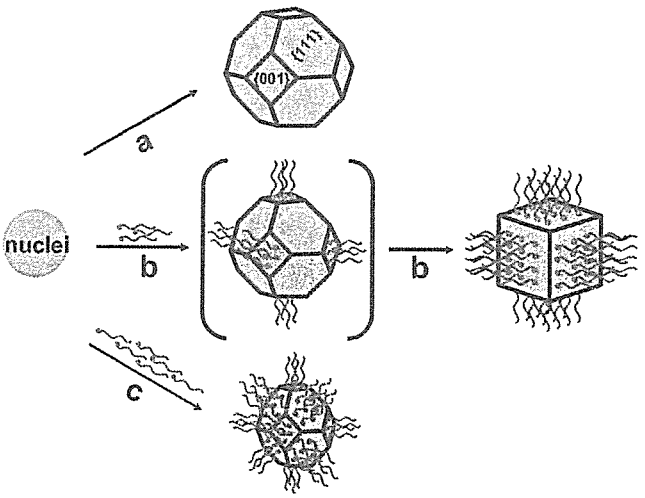

Figure 3. The shape control of ceria nanocrystals. a) A truncated octahedron in the case when no organic ligand molecules are used. b) At a low decanoic acid to ceria precursor ratio, the preferential interaction of the ligand molecules with the ceria {001} planes slows the growth of {001} faces relative to {111} faces, which leads to the formation of nanocubes. c) At a high decanoic acid to ceria precursor ratio, organic ligand molecules block growth on both {001} faces and {111} faces, which leads to the formation of truncated octahedra and smaller crystals.

because of the lower dielectric constant of water under supercritical conditions; the resulting homogenous phase also provided a suitable environment for the interaction of the organic ligand molecules with the surface of the ceria nanocrystals. Transformation of the shape of the ceria nanocrystals from truncated octahedral to cubic was mostly caused by the suppression of crystal growth on the (001) surface. As the CeO_2(001) surface is less stable than the (111) surface, the organic ligand molecules were likely to interact preferentially with the (001) surface: this greatly reduced the growth rate of the crystals in the ⟨001⟩ direction; crystal growth in the ⟨111⟩ direction became predominant. This change led to the formation of nanocubes with exposed (001) surfaces. When the amount of decanoic acid was further increased (molar ratio to ceria precursor, 24:1), the ceria nanocrystal size decreased to about 5 nm, as shown by the TEM image in Figure 2c. The HRTEM image (Fig. 2f) revealed that the nanocrystal shape was a truncated octahedron enclosed by the {111} and {200} planes. These results suggest that, at high organic ligand concentration, the organic ligand molecules can interact not only with the (001) surface but also with the (111) surface, and thus block crystal growth in both directions.

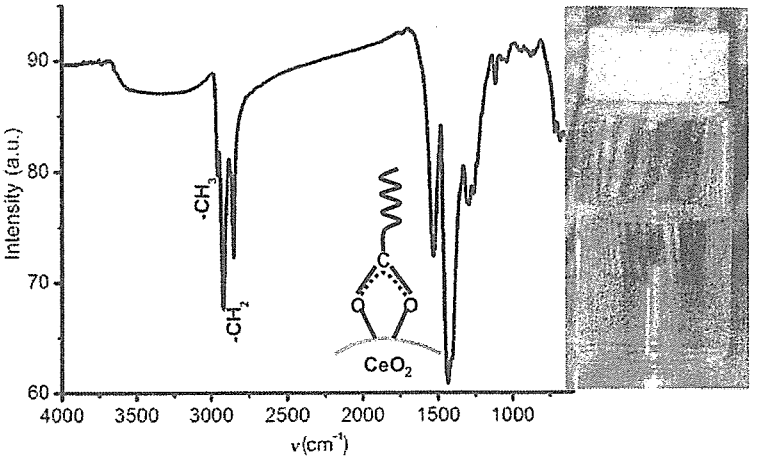

Figure 4. Left: The FTIR spectrum of ceria nanocrystals formed by decanoic acid assisted supercritical hydrothermal synthesis (the molar ratio of decanoic acid to ceria precursor is 24:1). Right: The transparent ceria nanocrystal with a concentration of 0.5 % (w/w) in THF.

As shown in Figure 2b and c, the 6 nm ceria nanocubes self assembled into approximately square packing on an amorphous carbon-coated TEM substrate, whereas the 5 nm truncated octahedron ceria crystals self assembled into hexagonal packing. The packing fashion is thought to be influenced by several factors, including the shape of the nanocrystals and the interaction between the organic ligand molecules, solvent, and substrate during the drying process.

To understand the interaction between the ceria nanocrystals and the organic ligand molecules, we analyzed the Fourier transform IR (FTIR) spectrum of ceria nanocrystals obtained from decanoic acid assisted supercritical hydrothermal synthesis. Bands in the 2800–2960 cm^{-1} region were attributed to the C–H stretching mode of methyl and methylene groups (Fig. 4). The bands at 1532 and 1445 cm^{-1} corresponded to the stretching frequency of the carboxylate group, which suggests that the carboxylate group from decanoic acid was chemically bonded to the surface of the ceria nanocrystals and the other hydrocarbon groups were oriented outward.[14] This is probably the result of reactions forming chemical bonds between the nanocrystal surface and the organic-ligand molecule in the unique reaction conditions of supercritical water, which are essential for the perfect dispersion of nanocrystals in organic solvents and for the arrangement of individual nanocrystals into superlattices.

In summary, our study offers a simple, rapid, and green chemistry approach to controlling the shape of ceria nanocrystals by tuning the interaction of organic molecules with various crystallographic planes of fluorite cubic ceria, using supercritical water as a reaction medium. Uniform nanocrystals bonding with the organic ligand molecules can be self assembled into close-packed superlattices on carbon substrates. These nanocrystals should find application in a variety of areas, including photonics and catalysis. Because of the convenience of the procedure and the ready availability of the chemicals used in this work, this route is expected to be applicable to a variety of metal (oxide) nanocrystals.

Experimental

Preparation of Ceria Nanocrystals: In a typical synthesis, the cerium oxide precursor was prepared by mixing 0.1 M $Ce(NO_3)_3$ solution (100 mL) with 0.3 M NaOH (100 mL). After the reaction mixture had been stirred for about 6 h, the precursor was centrifuged and washed several times with distilled water. Then, 2.5 mL of the 0.02 M precursor was transferred to a pressure-resistant SUS316 vessel (inner volume 5 mL). To modify the surface of the nanocrystals and induce their anisotropic growth, an appropriate amount of decanoic acid (0.05–1 g) was also loaded into the reactor vessel. The hydrothermal reaction was performed in the reactor at 400 °C for 10 min and terminated by submerging the reactor in a water bath at room temperature. The organic-ligand-modified nanocrystals were extracted from the product mixtures with hexane (3 mL). The final products were precipitated from the resulting hexane phase by the addition of ethanol (10 mL) as an antisolvent reagent, and then separated by using centrifugation. The obtained nanocrystals could be redissolved in some organic solvents such as hexane, toluene, and tetrahydrofuran (THF).

XRD, TEM, and HRTEM Measurements: The XRD patterns were recorded on a RINT-2000 spectrometer (Rigaku, Tokyo, Japan) with Cu Kα radiation. The samples were ground to fine powders before being subjected to XRD. The TEM images were obtained using a transmission electron microscope (JEM-1200EX, Japan) operated at 120 kV. The HRTEM characterization was carried out using a Hitachi H-7100 electron microscope operating at 200 kV. The samples for the TEM and HRTEM measurements were dispersed in THF before being transferred onto the carbon-coated copper grids.

Received: May 3, 2006
Revised: July 3, 2006

[1] T. Hyeon, S. S. Lee, J. Park, Y. Chung, H. B. Na, *J. Am. Chem. Soc.* **2001**, *123*, 2798.
[2] J. Rockenberger, E. C. Scher, A. P. Alivisatos, *J. Am. Chem. Soc.* **1999**, *121*, 11 595.
[3] J. Park, K. An, Y. Hwang, J. G. Park, H. J. Noh, J. Y. Kim, J. H. Park, N. M. Hwang, T. Hyeon, *Nat. Mater.* **2004**, *3*, 891.
[4] X. Wang, J. Zhuang, Q. Peng, Y. D. Li, *Nature* **2005**, *437*, 121.
[5] H. Weingartner, E. U. Franck, *Angew. Chem. Int. Ed.* **2005**, *44*, 2672.
[6] a) T. Adschiri, Y. Hakuta, K. Arai, *Ind. Eng. Chem. Res.* **2000**, *39*, 4901. b) T. Adschiri, K. Kanazawa, K. Arai, *J. Am. Ceram. Soc.* **1992**, *75*, 1019. c) T. Adschiri, K. Kanazawa, K. Arai, *J. Am. Ceram. Soc.* **1992**, *75*, 2615.
[7] K. J. Ziegler, R. C. Doty, K. P. Johnston, B. A. Korgel, *J. Am. Chem. Soc.* **2001**, *123*, 7797.
[8] P. S. Shah, T. Hanrath, K. P. Johnston, B. A. Korgel, *J. Phys. Chem. B* **2004**, *108*, 9574.
[9] A. Trovarelli, C. de Leitenburg, M. Boaro, G. Dolcetti, *Catal. Today* **1999**, *50*, 353.
[10] a) A. J. Zarur, J. Y. Ying, *Nature* **2000**, *403*, 65. b) R. Si, Y. W. Zhang, L. P. You, C. H. Yan, *Angew. Chem. Int. Ed.* **2005**, *44*, 3256. c) T. Y. Yu, J. Joo, Y. I. Park, T. W. Hyeon, *Angew. Chem. Int. Ed.* **2005**, *44*, 7411.
[11] a) D. C. Sayle, A. Maicaneanu, G. W. Watson, *J. Am. Chem. Soc.* **2002**, *124*, 11 429. b) K. B. Zhou, X. Wang, X. M. Sun, Q. Peng, Y. D. Li, *J. Catal.* **2005**, *229*, 206. c) M. Lundberg, B. Skarman, L. R. Wallenberg, *Microporous Mesoporous Mater.* **2004**, *69*, 187. d) H. X. Mai, L. D. Sun, Y. W. Zhang, R. Si, W. Feng, H. P. Zhang, H. C. Liu, C. H. Yan, *J. Phys. Chem. B* **2005**, *109*, 24 380.
[12] a) P. E. Savage, *Chem. Rev.* **1999**, *99*, 603. b) N. Akiya, P. E. Savage, *Chem. Rev.* **2002**, *102*, 2725.
[13] a) Z. L. Wang, *J. Phys. Chem. B* **2000**, *104*, 1153. b) Z. L. Wang, X. D. Feng, *J. Phys. Chem. B* **2003**, *107*, 13 563.
[14] a) V. Bolis, G. Magnacca, G. Cerrato, C. Morterra, *Thermochim. Acta.* **2001**, *379*, 147. b) C. Binet, M. Daturi, *Catal. Today* **2001**, *70*, 155. c) Y. G. Aronoff, B. Chen, G. Lu, C. Seto, J. Schwartz, S. L. Bernasek, *J. Am. Chem. Soc.* **1997**, *119*, 259. d) J. E. Tackett, *Appl. Spectrosc.* **1989**, *43*, 483.